Fracture toughness of soft materials with rate-independent hysteresis

Yuan Qi[1§], Julien Caillard[2§*], Rong Long[1*]

[1]Department of Mechanical Engineering, University of Colorado Boulder, Boulder, CO, 80309, USA.

[2]Manufacture Française des Pneumatiques Michelin, Centre de Technologies Europe, 63040 Clermont Ferrand Cedex 9, France.

§These two authors contributed equally to the paper.

*Corresponding authors: julien.caillard@michelin.com and rong.long@colorado.edu

Abstract

The fracture toughness of soft elastomers or gels can be substantially enhanced by introducing various energy dissipation mechanisms into the bulk material. Bulk dissipation, manifested in the hysteresis of loading-unloading cycles, enables the formation of a dissipation zone around the crack tip that consumes most of the energy provided by the external loading to drive crack propagation, effectively increasing the fracture toughness. An in-depth understanding on how bulk dissipation contributes to fracture toughness is required to predict crack propagation in soft materials with significant hysteresis. However, the current understanding is limited to the qualitative or empirical level due to the complex nonlinear mechanics involved in soft material fracture. This paper presents a theoretical framework for calculating the energy dissipation associated with crack propagation. To demonstrate its utility, we focus on steady state crack propagation and consider a model material system with rate-independent hysteresis: a neo-Hookean solid with Mullins effect. We determine analytical relations between fracture toughness and the parameters governing bulk hysteresis, and quantitatively predict the reduction in fracture toughness due to pre-stretch. Both agree well with finite element results. The framework presented here can be applied to a broader range of dissipative soft materials, thus providing a theoretical tool to guide the engineering of soft materials with high toughness.

Keywords: fracture toughness, crack tip field, dissipation, hysteresis, Mullins effect

1. Introduction

Soft materials that are resistant to fracture are highly desirable in a wide range of existing and emerging engineering applications, e.g. tires, sealants, pressure sensitive adhesives[1], soft robotics[2,3], biomedical implants[4] and stretchable electronics[5,6]. Experimental characterization of the fracture resistance involves the propagation of a macroscopic crack under controlled mechanical loadings. Specifically, the fracture toughness Γ (unit: J/m^2) is defined as the work required to advance the crack by a unit area. In reality, macroscopic cracks may originate from the growth and coalescence of small defects with various shapes and sizes. The effects of defects on fracture have been studied for many material systems[7–9]. For soft materials, a recent work by Chen et al.[10] showed that the toughness Γ, together with the bulk energy stored in the material at rupture, defines a critical length scale of defects below which the material becomes flaw insensitive, i.e., larger Γ implies that the material is less sensitive to defects. Therefore, Γ is an important parameter for evaluating a material's brittleness in general.

Tremendous research efforts have been devoted to enhancing the fracture toughness of soft elastomers or gels through various mechanisms such as sacrificial bond breaking[11–14], viscoelasticity[15,16], and particle fillers[17,18]. A common theme behind this diverse range of toughening mechanisms is bulk energy dissipation[19], which prevents the energetic driving force provided by external loadings from being fully delivered to the crack tip, thereby effectively enhancing the fracture toughness. For these dissipative materials, the toughness Γ can be divided into an intrinsic toughness Γ_0 and a term Γ_D representing the contribution due to bulk energy dissipation[19,20]:

$$\Gamma = \Gamma_0 + \Gamma_D \ . \tag{1}$$

Physically Γ_0 is associated with the material failure processes at the crack tip to create new surfaces. For example, Lake and Thomas[21] suggested that Γ_0 for crosslinked rubbery networks is the energy required to scission polymer chains per unit area. Unlike Γ_0, the physical processes underlying Γ_D occur at a much larger length scale, especially for soft materials with dramatically enhanced toughness[20]. Consequently, Γ_D can be much larger than Γ_0, and may become dependent on the size of fracture samples. In addition, Γ_D may depend on loading rates for viscoelastic materials. As a result, in general Γ_D cannot be regarded as a material property, and an accurate estimate of Γ_D is necessary for understanding the fracture of soft materials with strong dissipation.

Modeling Γ_D for soft materials is a challenging task. Early efforts were focused on viscoelastic materials, including the theoretical picture of viscoelastic "trumpet" proposed by de Gennes[16] and several more rigorous analyses[22–24]. These works are all based on linear viscoelasticity. More recently, Brown[25] and Tanaka[26] developed scaling models to understand Γ_D for double network gels with strong hysteresis. Although these works qualitatively captured the crack tip dissipation process, quantitative prediction of Γ_D still remains elusive. As pointed out in a couple of reviews[20,27], the nonlinearity associated with large deformation at crack tip plays a critical role in governing Γ_D for soft materials, but has rarely been addressed due to the lack of knowledge about the complex nonlinear deformation field in the crack tip region. Recently, Zhang et al.[28] made an encouraging progress in quantifying Γ_D for a tough hydrogel with rate-independent hysteresis. Based on scaling analysis and a finite element (FE) model that incorporated large deformation kinematics and a nonlinear damage model for the gel, they derived an analytical relation between Γ_D and bulk hysteresis parameters by fitting FE data. Despite its success, this approach relies on FE simulations and is empirical in nature. More theoretical insights that will enable a general strategy of calculating Γ_D for soft dissipative materials are yet to be established.

Here we present a theory to estimate Γ_D and Γ for Mode-I plane stress cracks under steady state propagation. Specifically, we focus on a simple material as a model system: a neo-Hookean hyperelastic solid with rate-independent hysteresis described by the Ogden-Roxburgh model for the Mullins effect[29]. Our goal is to derive analytical expressions for Γ_D and Γ based on theoretical considerations. Using this theory, we can also predict the reduction in toughness Γ due to pre-stretch which reduces bulk dissipation. This paper is organized as follows. In Section 2, we present the basic elements of our theory to estimate Γ_D. In Section 3, we consider two limiting cases for estimating Γ_D based on which an expression for intermediate cases is constructed and compared to finite element results. Moreover, we discuss in Section 4 the reduction in fracture toughness due to pre-stretch. We conclude in Section 5 with a summary of our work followed by additional discussions.

2. Energy release rate

According to the Griffith's fracture criterion, crack propagation would occur when $G \geq \Gamma$, where G is the energy release rate. For linear elastic materials, G is defined as the potential energy, consisting of strain energy stored in the material and potential energy of the loading system, to be released if the crack grows by a unit area. For soft dissipative materials, two aspects of this definition need to be clarified. First, since soft materials can undergo large deformation which may cause a significant change in area as the crack deforms, the crack area to define G (or Γ) usually refers to the area in the undeformed configuration, which will be adopted in this paper. Second, for soft dissipative materials, the strain energy is not well defined since the material exhibits hysteresis during loading and unloading. In this section, we start with a rigorous definition of energy release rate for materials with hysteresis, and then specialize it for steady state crack propagation and the neo-Hookean solid with Mullins effect.

2.1 Energy release rate for materials with hysteresis

Let us consider a volume V delimited by a surface Ω. This volume of material is subjected to external loading, and a crack of surface area A can propagate in it. These geometrical entities are all defined with respect to the undeformed configuration. Next we examine the energy exchange between this volume and its environment during crack propagation. All quantities used in the derivation below are with respect to the undeformed configuration.

The internal energy E contained in V can be affected by external loading, heat exchange, and crack propagation. Assuming quasi-static crack propagation so that equilibrium is always satisfied (i.e., no inertial term to be accounted for) and no body forces, we obtain the following energy balance equation for dE/dt (t stands for time):

$$\frac{dE}{dt} = \int_{\Omega} \mathbf{T} \cdot \frac{d\mathbf{u}}{dt} d\Omega + \int_{V} \left(\omega - \nabla_{\mathbf{X}} \cdot \mathbf{q} \right) dV - E_0 \frac{dA}{dt} \ . \tag{2}$$

The first term on the right hand side of eq.(2) represents the power supplied by external loading, where **T** and **u** are traction and displacement vectors on Ω. The second term represents the rate of heat exchange with the environment[30], where ω is the rate of external heat supply per unit volume, **q** is the heat flux vector, and $\nabla_{\mathbf{X}}$ is the gradient operator. The third term accounts for the power consumed by crack propagation, where E_0 is the internal energy required to break a unit area of material (unit: $\mathrm{J \cdot m^{-2}}$). Physically E_0 should be a function of the loading conditions at the crack tip, e.g. the temperature and crack propagation rate.

In a similar manner, we can write the following equation for the entropy Σ contained in *V*:

$$\frac{d\Sigma}{dt} = \int_V \left(\frac{\omega}{\theta} - \nabla_{\mathbf{X}} \bullet \left(\frac{\mathbf{q}}{\theta} \right) \right) dV + \int_V \frac{\gamma}{\theta} dV - \Sigma_0 \frac{dA}{dt} \ . \tag{3}$$

The first term on the right hand side of eq.(3) is the entropy change due to heat exchange, where θ (≥ 0) is the absolute temperature. The second term represents the entropy increase due to irreversible phenomena in the solid, where γ is the energy dissipation per unit volume. The second law of thermodynamics dictates that $\gamma \geq 0$. The third term accounts for the contribution due to crack propagation, where Σ_0 is the entropy change associated with the breaking of a unit area of material (unit: $\mathrm{J \cdot m^{-2} \cdot K^{-1}}$). Similar to E_0, Σ_0 depends on loading conditions at the crack tip and is in general not a material constant.

Since eq.(3) holds for any volume enclosing the crack tip, it can be rewritten exclusively in terms of volume integrals. For example, the entropy Σ can be written as volume integrals of σ, which is the entropy per unit volume. The term $\Sigma_0 \mathrm{d}A/\mathrm{d}t$ can be written as the volumetric integral of $\Sigma_0 \mathrm{d}A/\mathrm{d}t$ multiplied by a Dirac delta function centered at the crack tip. As a result, the global entropy equation of eq.(3) can be recast into local forms in terms of partial differential equations. Multiplying the local form of eq.(3) by temperature θ and integrating over *V*, we get

$$\int_V \theta \frac{d\sigma}{dt} dV = \int_V \left[\omega - \nabla_{\mathbf{X}} \bullet \mathbf{q} + \gamma + \frac{\mathbf{q} \bullet \nabla_{\mathbf{X}} \theta}{\theta} \right] dV - \theta_0 \Sigma_0 \frac{dA}{dt} \ , \tag{4}$$

where θ_0 is the temperature at the crack tip and we have used the identity that $\nabla_{\mathbf{X}} \bullet (\mathbf{q}/\theta) = (\nabla_{\mathbf{X}} \bullet \mathbf{q})/\theta - \mathbf{q} \bullet \nabla_{\mathbf{X}}\theta/\theta^2$.

Subtracting eq.(4) from eq.(2) and rearranging, we obtain

$$\int_{\Omega} \mathbf{T} \bullet \frac{d\mathbf{u}}{dt} d\Omega - \int_{V} \left(\frac{de}{dt} - \theta \frac{d\sigma}{dt} \right) dV - \left(E_0 - \theta_0 \Sigma_0 \right) \frac{dA}{dt} = \int_{V} \left[\gamma + \frac{\mathbf{q} \bullet \nabla_{\mathbf{X}}\theta}{\theta} \right] dV , \tag{5}$$

where e is the internal energy per unit volume. Let φ denote the integrand on the right hand side of eq.(5). When the temperature field is homogeneous, $\varphi = \gamma$ and so $\varphi \geq 0$. Otherwise we assume Fourier's law in the reference configuration, $\mathbf{q} = -\kappa \nabla_{\mathbf{X}}\theta$ with $\kappa \geq 0$. Consequently, $\varphi = \gamma - \kappa \, |\nabla_{\mathbf{X}}\theta|^2 / \theta$, where the term after the minus sign, manifestly positive, represents the dissipation rate accompanying heat conduction. Therefore, φ can be interpreted as the rate of purely mechanical dissipation, also referred to as the intrinsic dissipation. The second law of thermodynamics, represented by the constraint that $\gamma \geq 0$, dictates that $\varphi \geq 0$ under the isothermal condition. Moreover, introducing the Helmholtz free energy density $\psi \equiv e - \theta\sigma$ and remembering that $\sigma = -\partial\psi/\partial\theta$, we see that

$$\frac{de}{dt} - \theta \frac{d\sigma}{dt} = \frac{d\psi}{dt} - \left(\frac{\partial \psi}{\partial \theta} \right) \frac{d\theta}{dt} = \left. \frac{d\psi}{dt} \right|_{\theta} , \tag{6}$$

where the last notation indicates a time derivative at constant temperature θ. Lastly, we note that $(E_0 - \theta_0\Sigma_0)$ in eq.(5) is the Helmholtz free energy required to advance the crack per unit area, and thus is recognized as the intrinsic fracture toughness $\Gamma_0 \equiv E_0 - \theta_0\Sigma_0$. Instead of enforcing that Γ_0 is a material constant, we retain the generality that Γ_0 may depend on local conditions at the crack tip (e.g. temperature or crack propagation rate[31]). Defining the total Helmholtz free energy as $\Psi \equiv \int_V \psi \, dV$, eq.(5) becomes

$$\int_{\Omega} \mathbf{T} \bullet \frac{d\mathbf{u}}{dt} d\Omega - \left. \frac{d\Psi}{dt} \right|_{\theta} - \Gamma_0 \frac{dA}{dt} = \int_{V} \varphi dV . \tag{7}$$

The dissipation rate φ can be determined by using the local form of eq.(7) in an arbitrary sub-volume V^* that does not contain the crack tip so that the term associated with Γ_0

vanishes. Specifically, assuming no body forces, we apply the traction-stress relation and the equilibrium equation in this arbitrary sub-volume V^*, and can derive that[30]

$$\int_{\Omega^*} \mathbf{T} \bullet \frac{d\mathbf{u}}{dt} d\Omega = \int_{V^*} \mathbf{S} : \frac{d\mathbf{F}}{dt} dV \ , \tag{8}$$

where **S** is the first Piola-Kirchhoff stress tensor, **F** is the deformation gradient tensor and Ω^* is the boundary of V^*. Using eq.(8), we obtain the following expression for φ:

$$\varphi = \mathbf{S} : \frac{d\mathbf{F}}{dt} - \left.\frac{d\psi}{dt}\right|_{\theta} \ . \tag{9}$$

For an elastic material, the free energy density ψ depends only on **F** under a fixed temperature with $\mathbf{S} = \partial\psi/\partial\mathbf{F}$, and therefore $\varphi = 0$. For materials with dissipation, ψ and **S** may depend on multiple internal variables which are governed by the deformation history. In this case, we expect $\varphi > 0$.

The derivation above is based on the assumption of quasi-static crack growth with equilibrium. This implies $G_0 = \Gamma_0$ where G_0 is the intrinsic energy release rate for driving the fracture processes at crack tip. In addition, we note that the global energy release rate G is defined by the change in potential energy Π per unit area of crack growth[32], i.e.,

$$G = -\frac{\partial \Pi}{\partial A} = \int_{\Omega} \mathbf{T} \bullet \frac{\partial \mathbf{u}}{\partial A} d\Omega - \left.\frac{\partial \Psi}{\partial A}\right|_{\theta} \ . \tag{10}$$

To establish a connection between G_0 and G, we expand the time derivatives of **u** and Ψ in eq.(7) into two parts: one due to the growth in crack area A (i.e., $(\partial ... /\partial A)\ \mathrm{d}A/\mathrm{d}t$), and the other due to time dependent processes occurring at constant A (i.e., $(\partial ... /\partial t)|_A$). The latter can result from changing external loading conditions or from viscoelastic relaxation/creep under constant external loading. Using eq.(10) and $G_0 = \Gamma_0$, we can rewrite eq.(7) as

$$\left(G - G_0\right)\frac{dA}{dt} + \int_{\Omega} \mathbf{T} \bullet \left.\frac{\partial \mathbf{u}}{\partial t}\right|_A d\Omega - \left.\frac{\partial \Psi}{\partial t}\right|_{\theta, A} = \int_V \varphi dV \ . \tag{11}$$

This is the general energy balance equation we were looking for. It connects the dissipative energy release rate $G_D \equiv G - G_0$ with the bulk dissipation rate φ, and is valid for any dissipative material models including the rate dependent ones (e.g. viscoelasticity).

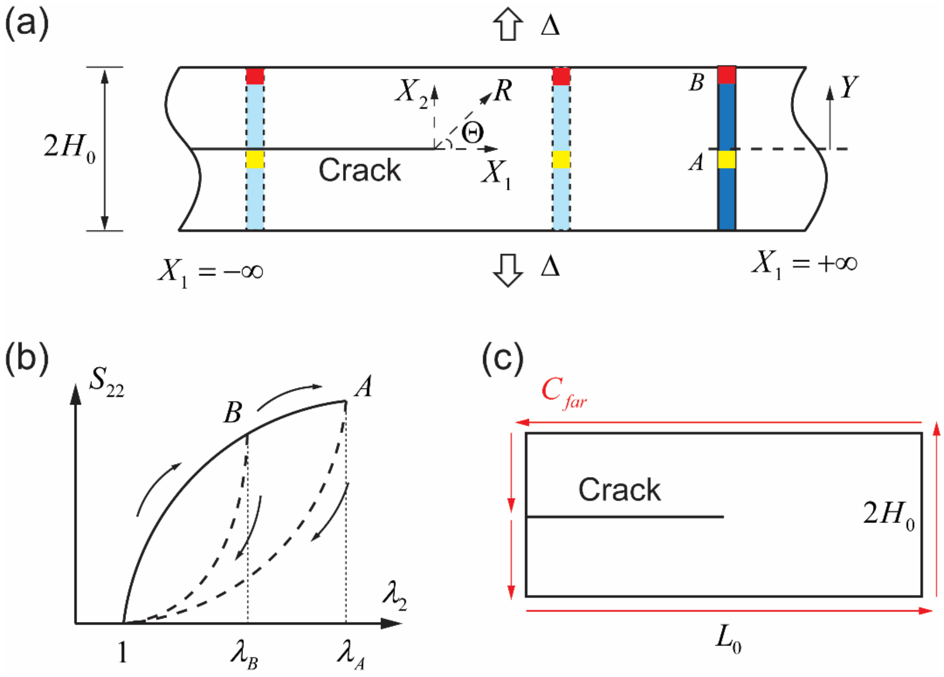

Figure 1 (a) Schematic of steady state crack propagation in a pure shear fracture test (shown in the reference configuration). With respect to a translating coordinate system X_1-X_2 centered at the crack tip, crack propagation is equivalent to moving a vertical strip from $X_1 = +\infty$ to $= -\infty$. A and B are two different points along the vertical strip. (b) The different loading histories experienced by the two points A and B illustrated using the dominating stress and deformation components for a Mode-I crack, i.e. S_{22} versus λ_2. The maximum stress experienced by A is larger due to stress concentration at the crack tip. (c) Integration path C_{far} is along perimeter of the fracture specimen.

2.2 Steady-state propagation of a plane stress crack

To put eq.(11) into the perspective of this work, here we consider a special case: steady-state Mode-I crack propagation in a pure shear fracture specimen with isothermal condition. The pure shear geometry was first developed by Rivlin & Thomas[33] and has been widely used to characterize the fracture toughness of soft materials[12,13,34]. Figure 1a shows the pure shear geometry when mapped back to the undeformed configuration. The lateral dimension of the sample is much larger than the height ($2H_0$) and is considered to be infinite here for theoretical purpose. To drive crack propagation, the top and bottom boundaries are clamped and subjected to a displacement loading of 2Δ along the vertical direction. The displacement loading is often represented using the stretch ratio far ahead of the crack tip:

$$\lambda = 1 + \frac{\Delta}{H_0} \ . \tag{12}$$

Steady state crack propagation implies that under a fixed λ_s, the stress and strain fields in the fracture sample are translationally invariant[35]. To use this condition, we set up a translating coordinate system X_1-X_2 that is centered at the crack tip and translates with the crack. The stress and strain fields expressed in terms of X_1-X_2 are independent of the crack length a measured from the origin of a fixed coordinate system.

For this plane stress crack, $A = at_0$ where t_0 is the thickness of the specimen and a is the crack length. Since the displacement loading is fixed, the boundary integral term in eq.(10) vanishes. In addition, the steady state condition implies that $\partial\ldots/\partial A = -(1/t_0)\ \partial\ldots/\partial X_1$, which implies

$$G = \int_{-H_0}^{H_0}\int_{-\infty}^{+\infty} \frac{\partial \psi}{\partial X_1} dX_1 dX_2 = \int_{-H_0}^{H_0} \left[\psi\left(X_1 = +\infty\right) - \psi\left(X_1 = -\infty\right)\right] dX_2 \ . \tag{13}$$

It is worth noting that the expression of G in eq.(10) can be rewritten as a contour integral for steady state two dimensional (2D) crack propagation (see Appendix 1 for a detailed derivation):

$$G = \int_{C_{far}} \left(\psi \mathbf{e}_1 - \mathbf{S}^T \frac{\partial \mathbf{u}}{\partial X_1} \right) \bullet \mathbf{N} dl = \int_{C_{far}} \Xi_{1j} N_j dl \ , \tag{14}$$

where $\Xi_{ij} = \psi\delta_{ij} - S_{kj}\partial u_k / \partial X_i$. In eq.(14), the contour C_{far} is along perimeter of the fracture specimen (see Fig.1c), $\mathbf{e}_1$ is the unit vector along X_1, $\mathbf{N}$ is the unit outward normal vector of the contour C_{far}, and δ_{ij} is the Kronecker delta operator. The indices (i, j, k) range from 1 to 2, and the Einstein summation convention of summing over repeated indices is adopted. Applying eq.(14) to the pure shear fracture geometry also results in eq.(13). We recognize that Ξ_{ij} are components of the Eshelby energy momentum tensor[36,37] but in an inelastic context. Moreover, we have recovered the well-known J-integral through eq.(14). Unlike elastic materials where the J-integral is proved to be path-independent, in general the contour integral in eq.(14) is expected to be path-dependent due to dissipation, and thus the contour C_{far} must be the perimeter of the fracture specimen. However, if dissipation is concentrated in a small zone surrounding the crack tip, the contour C_{far} can be made smaller as long as it encloses the dissipation zone. Note that in some literature[38], the deformation gradient $F_{ki} = \delta_{ki} + \partial u_k/\partial X_i$ is used instead of $\partial u_k/\partial X_i$ in the definition of Ξ_{ij}, which adds an additional S_{ij} to Ξ_{ij}. This however does not affect G by enforcing equilibrium in the absence of body forces.

Next we consider $G_D = G - G_0$ in eq.(11). In addition to the steady-state condition with fixed loading, we further assume the material behavior is rate-independent. In this case, the partial time derivatives $(\partial\ldots/\partial t)|_A$ in eq.(11) vanish identically, and we have

$$G_D = G - G_0 = \int_{-H_0}^{H_0}\int_{-\infty}^{+\infty} \frac{\varphi}{v_p} dX_1 dX_2 \ , \tag{15}$$

where $v_p = \mathrm{d}a/\mathrm{d}t$ is the crack propagation velocity and we have set $\mathrm{d}A/\mathrm{d}t = t_0 v_p$. To use the dissipation rate φ given in eq.(9), we first use the steady-state condition to simplify the time derivatives, i.e., $(\mathrm{d}\ldots/\mathrm{d}t) = (\partial\ldots/\partial A)\,\mathrm{d}A/\mathrm{d}t = -(\partial\ldots/\partial X_1)\,v_p$, which results in

$$\frac{\varphi}{v_p} = -\mathbf{S} : \frac{\partial \mathbf{F}}{\partial X_1} + \left.\frac{\partial \psi}{\partial X_1}\right|_{\theta} \ , \tag{16}$$

so that

$$G_D = \int_{-H_0}^{H_0}\int_{-\infty}^{+\infty} \left(-\mathbf{S} : \frac{\partial \mathbf{F}}{\partial X_1} + \frac{\partial \psi}{\partial X_1} \right) dX_1 dX_2 = \int_{-H_0}^{H_0} \left[\int_{\mathbf{F}(X_1=+\infty)}^{\mathbf{F}(X_1=-\infty)} \mathbf{S} : d\mathbf{F} - d\psi \right] dX_2 \ . \tag{17}$$

We have dropped the fixed temperature constraint for $\partial\psi/\partial X_1$ due to the isothermal assumption. Equation (17) is the basis for the remainder of our article. It states that the dissipative energy release rate G_D can be calculated by imaginarily moving a material point at $X_1 = +\infty$ horizontally (i.e. at a fixed X_2) to $X_1 = -\infty$ and integrating the bulk dissipation along this deformation history. As pointed out in Long & Hui[35], the material points at different X_2 experience different deformation histories. For example, in Fig.1b we use the dominating stress and deformation components, i.e. S_{22} versus λ_2 due to the Mode-I condition, to schematically illustrate the deformation history of two material points A and B. Due to stress concentration at the crack tip, point A would first experience additional loading as it approaches the crack tip before unloading occurs. In contrast, since the global stretch ratio λ_s is fixed, point B near the top boundary would only experience unloading as it is moved from $X_1 = +\infty$ to $X_1 = -\infty$.

Before specializing G_D for a material model with Mullins effect, it is worth mentioning that the formalism of "material forces" associated with the manipulation of Eshelby energy momentum tensor (see for example Grellmann et al.[39] pp. 192-202 for a short review) also leads to eq.(17), as demonstrated in Appendix 1.

2.3 Material model: neo-Hookean solid with Mullins effect

We adopt the same material model used in Zhang et al.[28] which consists of two components: i) the incompressible neo-Hookean model to describe the initial loading response and ii) the modified Ogden-Roxburgh model[29] to phenomenologically describe the softening behavior associated with Mullins effect. With this model and assuming isothermal condition, the free energy density ψ is given by

$$\psi = \eta W(\mathbf{F}) \quad \text{and} \quad W(\mathbf{F}) = \frac{\mu}{2}(\lambda_i \lambda_i - 3) , \tag{18}$$

where μ is the shear modulus at infinitesimal strain, λ_i (i =1,2,3) are the three principal stretch ratios, η is the damage variable ($0 \leq \eta \leq 1$) and W will be referred to as the nominal strain energy density. The first Piola-Kirchhoff stress tensor $\mathbf{S}$ is given by

$$\mathbf{S} = \eta \frac{\partial W}{\partial \mathbf{F}} - p\mathbf{F}^{-T} , \tag{19}$$

where p is a Lagrange multiplier to enforce the incompressibility constraint. According to the modified Ogden-Roxburgh model[28], the damage variable η is given by

$$\eta = 1 - \frac{1}{r} erf\left(\frac{W_{\max} - W}{m + \beta W_{\max}} \right), \tag{20}$$

where *erf* stands for the error function and the parameters r, m and β are material constants. As shown in eq.(18), W is associated with the current deformation state $\mathbf{F}$, while W_{max} is the maximum of W experienced by the material point along the deformation history. During the initial loading, $\eta=1$ since $W=W_{max}$, and the material behaves as a hyperelastic solid with W being the strain energy density. Take uniaxial tension as an example: W is equal to the area underneath the stress-stretch curve during initial loading (see Fig.2a). When unloading occurs, $W<W_{max}$ and thus $\eta<1$, and hence the softening behavior during unloading can be captured. Unlike the pseudo-elastic model of Odgen and Roxburgh[29] where an additional damage function is added to ψ so that the dissipation rate $\varphi=0$, we follow the approach in Holzapfel[30] and adopt the form in eq.(18) to retain the dissipation term φ.

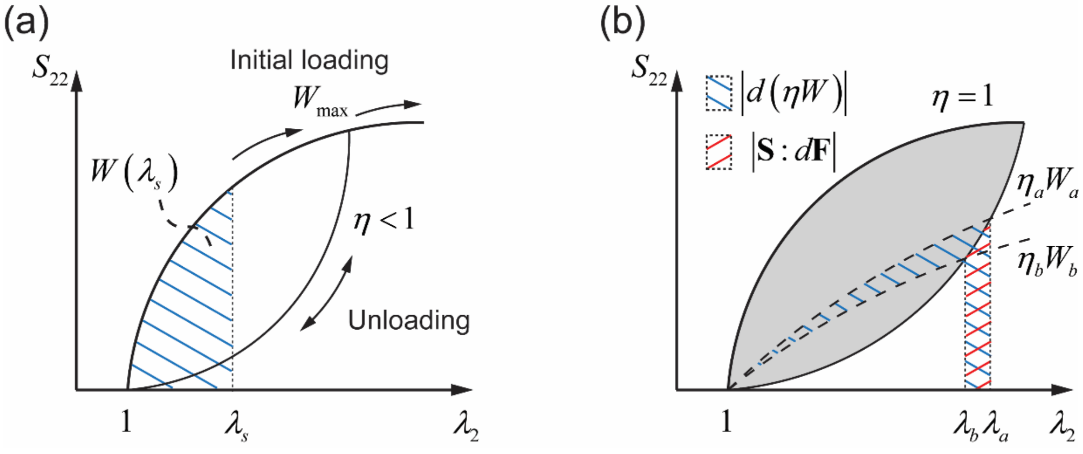

Figure 2 (a) Hysteresis due to the Mullins effect illustrated by the stress versus stretch ratio curve under uniaxial tension. The area underneath the initial loading curve is defined as the nominal strain energy density W. (b) Illustration of the incremental dissipation $dU=\mathbf{S}:d\mathbf{F}-d\psi$. Along the initial loading curve $dU=0$ and during unloading $dU>0$. The areas representing $|d\psi|=-d(\eta W)$ and $|\mathbf{S}:d\mathbf{F}|=-\mathbf{S}:d\mathbf{F}$ for a small segment along the unloading branch are highlighted, and dU is represented by the shaded strip within the hysteresis loop.

This material model allows us to further simplify the expression for G in eq.(13) and G_D in eq.(17). First, the material model in eq.(18) implies that there is no permanent deformation when the material is completely unloaded. Therefore, at $X_1=-\infty$ (far behind the crack tip), the material returns to the undeformed configuration and $\psi(X_1=-\infty)=0$.

At $X_1 = +\infty$ (far ahead of crack tip), the material has only experienced initial loading (i.e., $\eta = 1$), and is under pure shear extension with the principal stretch ratios being $\lambda_1 = 1$, $\lambda_2 = \lambda_s$ and $\lambda_3 = 1/\lambda_s$ where we have assumed incompressibility. Therefore, $\psi(X_1 = +\infty) = \mu(\lambda_s^2 + \lambda_s^{-2} - 2) \equiv W_{far}$, and eq.(13) becomes

$$G = 2H_0 W_{far} \ , \tag{21}$$

which has been widely used to evaluate energy release rate and fracture toughness in pure shear fracture tests[12,13,34].

Next we consider G_D. Using eqs.(18) and (19), we find the integrand in eq.(17) to be

$$\mathbf{S} : d\mathbf{F} - d\psi = \eta dW - d\left(\eta W\right) = -W d\eta \, , \tag{22}$$

where we have used the incompressibility condition that $J = \det(\mathbf{F}) = 1$ and the Jacobi's formula that $\mathbf{F}^{-\mathrm{T}} : d\mathbf{F} = dJ/J = 0$. The incremental dissipation $\mathbf{S}:\mathrm{d}\mathbf{F} - \mathrm{d}\psi$ in eq.(22) is zero during initial loading since $\eta = 1$, and is positive during unloading since $\mathrm{d}\eta < 0$. It should be noted that this model is not thermodynamically consistent during a second reloading, since $-W\mathrm{d}\eta < 0$ which implies a negative dissipation rate ($\varphi < 0$) during reloading and thus violates the second law of thermodynamics. This inconsistency is due to the phenomenological nature of the damage evolution law in eq.(20), which is adopted to enable comparison with previous results in the literature[28]. It does not affect our analysis in Section 3 since all material points experience only one loading and one unloading. However, reloading would occur if the material experienced a pre-stretch before crack propagation, which will be considered in Section 4. In this case, we will not be able to apply the thermodynamic framework directly; instead, our analysis will be based on physical arguments regarding the mechanical work and dissipation. Further discussions on an alternative damage evolution law for η, which is thermodynamically consistent, are provided in Section 5.

Defining U as the energy dissipation per unit volume as a material point is translated from $X_1 = +\infty$ to $X_1 = -\infty$, we can write

$$U=\int_{\mathbf{F}(X_1=+\infty)}^{\mathbf{F}(X_1=-\infty)}\left(\mathbf{S}:d\mathbf{F}-d\psi\right)=-\int_{\mathbf{F}(X_1=+\infty)}^{\mathbf{F}(X_1=-\infty)}Wd\eta\ , \tag{23}$$

Since dη=0 along the loading curve, the integration limit in eq.(23) can be adjusted so that it only covers the unloading branch, i.e., W ranging from W_{max} to 0:

$$U=-\int_{W_{\max}}^{0}Wd\eta=W_{\max}-\int_{0}^{W_{\max}}\eta dW=\int_{0}^{W_{\max}}(1-\eta)\,dW\ . \tag{24}$$

Physically U is represented by the area of the hysteresis loop in Fig.2b. To further illustrate this equation, we look at two neighboring points along the unloading branch of S_{22}-λ_2 curve. The incremental work −**S**:d**F** is the area shaded in red lines, which is a subset of the area representing −dψ or –d(ηW) (shaded in blue lines). The complement of these two areas, which is equal to dU=−dψ− (−**S**:d**F**), forms a strip within the hysteresis loop. Adding up these strips along the unloading branch gives the entire area of the hysteresis loop, which is highlighted in gray in Fig.2b and expressed mathematically in eq.(24). Substituting eq.(20) into eq.(24), we can obtain an analytical expression for U (W_{max}), based on which we define the hysteresis ratio h as:

$$h\left(W_{\max}\right)=\frac{U\left(W_{\max}\right)}{W_{\max}}=\frac{1}{r}\left[erf\left(\frac{1}{\beta+m/W_{\max}}\right)+\frac{1}{\sqrt{\pi}}\left(\beta+m/W_{\max}\right)\left(e^{\frac{-1}{\left(\beta+m/W_{\max}\right)^2}}-1\right)\right]. \tag{25}$$

As discussed earlier, the W_{max} experienced by a material point depends on its vertical position X_2 along the strip shown in Fig.1a. Using eqs.(17), (23)-(25), we finally arrive at the following equation:

$$G_D=2\int_0^{H_0}UdY=2\int_0^{H_0}h\left(W_{\max}\right)W_{\max}\left(Y\right)dY\ , \tag{26}$$

where we have renamed the vertical coordinate X_2 to Y to clarify notation, and applied the symmetry condition about Y =0. Similar expression for G_D was developed in Long & Hui[35] based on physical arguments. Here we provide a rigorous derivation from a more general thermodynamic definition of energy release rate.

3. Dissipation and toughness

In this section we focus on determining the relationship between the toughness Γ and its dissipative component Γ_D. To use the expressions for energy release rates derived in Section 2, especially eq.(26) for G_D, we assume the intrinsic toughness Γ_0 is a known material constant and prescribe a local fracture criterion at the crack tip, i.e., $G_0 = \Gamma_0$. The G_D and G associated with this local fracture criterion are then equal to Γ_D and Γ, respectively. Now the question is: how do we calculate G_D?

3.1 Analytical model

The first step to calculate G_D is to determine the function $W_{max}(Y)$ in eq.(26), which depends on the nonlinear deformation field around the crack tip. We start by considering an ***elastic*** neo-Hookean solid for which the crack tip deformation field has been solved asymptotically. Specifically, the first order terms of the dominant deformation gradient components are[40]:

$$F_{21} = -\frac{B}{2} R^{-1/2} \sin\left(\Theta/2\right) \quad and, \quad F_{22} = \frac{B}{2} R^{-1/2} \cos\left(\Theta/2\right), \tag{27}$$

where R and Θ are polar coordinates in the reference configuration (centered at the crack tip, see Fig. 1a) and B is an undetermined coefficient specifying the amplitude of the crack tip field. Note that in the crack tip region the other non-zero deformation gradient components, i.e. F_{11}, F_{12} and F_{33}, are all negligible in comparison to F_{21} and F_{22}. Substituting eq.(27) into eq.(18), and remembering that $\lambda_i\lambda_i = F_{ij}F_{ij}$ we obtain the following distribution of W around the crack tip:

$$W = \frac{\mu B^2}{8}\frac{1}{R} = \frac{\mu B^2}{8}\frac{1}{Y}\sin\Theta \quad \left(Y > 0\right), \tag{28}$$

where we have used the identity that $Y = R\sin\Theta$. The amplitude B of the local crack tip field can be related to the external loading, represented by the global energy release rate G, by calculating the J-integral. Using the result in Long & Hui[40], we find

$$G = J = \frac{\mu\pi}{4} B^2. \tag{29}$$

Combing eqs.(28) and (29), we can write

$$W = \frac{G}{2\pi}\frac{1}{Y}\sin\Theta \ . \tag{30}$$

According to the definition in Section 2.3, W_{max} is the maximum of W as a material point is translated from $X_1 = +\infty$ to $X_1 = -\infty$, which corresponds to a fixed Y and Θ ranging from 0 to π. Hence $W_{max}(Y)$ has the following form:

$$W_{\max}\left(Y\right) = \frac{G}{2\pi}\frac{1}{Y} . \tag{31}$$

It should be emphasized that eq.(31) was derived based on the first order asymptotic solution of the crack tip field. In principle, it should only be valid very close to the crack tip (within the region of validity for eq.(27)). However, from the perspective of scaling analysis, W_{max} should be proportional to G according to the J-integral. In the limit of $H_0 \to \infty$, Y is the only relevant length scale, and dimensional analysis dictates that $W_{max} \sim G/Y$. Therefore, we hypothesize that eq.(31) has a larger region of validity than the asymptotic solution in eq.(27), and is applicable throughout the sample except near the top and bottom boundaries $Y = \pm H_0$.

To account for the boundary effect near $Y = H_0$, we note that the material point at $Y = H_0$ would only experience unloading as it is translated from $X_1 = +\infty$ to $X_1 = -\infty$ since the applied stretch λ is fixed. Therefore, using eq.(21) we obtain

$$W_{\max}\left(Y = H_0\right) = W_{far} = \frac{G}{2H_0} \ , \tag{32}$$

which implies eq.(31) is not valid near $Y = \pm H_0$. Otherwise we would get $W_{max}(Y=H_0) = G/(2\pi H_0)$ which is inconsistent with eq.(32). To reconcile eqs.(31) and (32), we hypothesize that eq.(31) is only valid for $0 < Y \leq H_0/\pi$, and W_{max} becomes uniform when Y exceeds H_0/π, as schematically shown in Fig.3. The actual transition from eq.(31) to eq.(32) may not be as sharp as assumed in Fig.3b. However, Fig.3b can capture the essential features of $W_{max}(Y)$ without evoking a complex analysis of the deformation field.

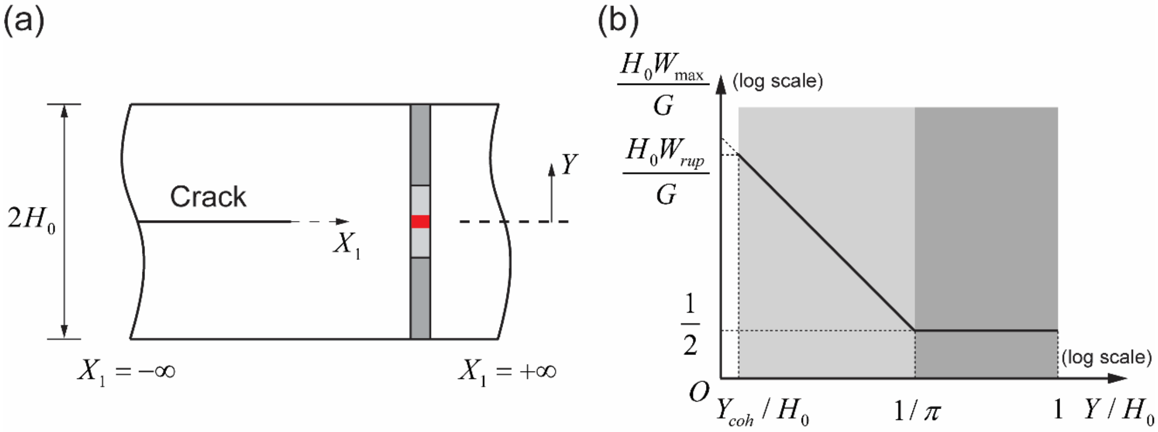

Figure 3 The function $W_{\max}$ (Y). (a) The vertical strip used to evaluate G_D. (b) Schematic of $W_{\max}$ (Y) plotted in log-log scale. The vertical strip is divided into 3 parts: fracture process zone near Y=0 (red), a region where W_{max}~1/Y for intermediate |Y|, constant W_{max} for |Y| close to H_0.

The theoretical picture sketched above is derived for the elastic neo-Hookean solid. When the Mullins effect is introduced, the crack tip deformation field may be distorted by the hysteresis. However, since W_{max} is the maximum W along the loading history of a material point at Y and the loading branch follows the neo-Hookean model, we hypothesize the $W_{max}(Y)$ shown in Fig.3 can be applied, at least approximately, to eq.(26) for estimating G_D. We will evaluate the accuracy of this hypothesis using finite element results later and make corrections if necessary. For the time being eq.(26) becomes

$$G_D = \frac{G}{\pi} \int_0^{H_0/\pi} h\left(W_{\max}\right) \frac{dY}{Y} + G\left(1 - \frac{1}{\pi}\right) h\left(\frac{G}{2H_0}\right) \tag{33}$$

A difficulty is encountered in the first integral of eq.(33) at the crack tip Y =0. This is due to singularity of W_{max} as $Y \to 0$, which can be regularized by considering a fracture process zone at the crack tip. The energy required to drive the fracture process is represented by the intrinsic toughness Γ_0. In numerical simulations the process zone is usually incorporated using a cohesive zone model as described in Section 3.2. The distribution of W_{max} in a small region adjacent to the cohesive zone would deviate from eq.(31). Assuming the process zone is much smaller than characteristic length scale of the fracture sample (e.g. H_0), we implement a cut-off in W_{max} denoted by W_{rup}, i.e., the nominal strain energy density when rupture occurs. This allows us to neglect the contribution to G_D from the process zone due to its small volume. The cut-off W_{rup} corresponds to a length scale of the cohesive zone, defined as $Y_{coh} = G/(2\pi W_{rup})$, that is much smaller than H_0. After implementing the cut-off and the change of variable $dW_{max}/W_{max} = -dY/Y$ in the first integral of eq.(33), we obtain:

$$\frac{G_D}{G} = \frac{1}{\pi} \int_{G/(2H_0)}^{W_{rup}} h\left(W_{\max}\right) \frac{dW_{\max}}{W_{\max}} + \left(1 - \frac{1}{\pi}\right) h\left(\frac{G}{2H_0}\right) . \tag{34}$$

This equation reveals the connection between G_D and bulk dissipation due to the Mullins effect manifested in the hysteresis ratio h given in eq.(25). By replacing G_D with $G - G_0$, it also allows us to solve for the total toughness Γ (= G) and dissipative toughness Γ_D (=G_D) for prescribed values of H_0, W_{rup} and $G_0 = \Gamma_0$. In addition, we observe that in general the ratio G_D/G depends on the fracture sample size H_0 and the cut-off W_{rup}.

Two questions remain to be answered. First, how accurate is the approximation of applying the $W_{max}(Y)$ for an elastic model to a solid with hysteresis? Second, how can we obtain analytical results of G_D/G using the nonlinear function of $h(W_{max})$. For the first question, we will use a finite element model, following the approach of Zhang et al.[28], to verify the approximation and to motivate modifications. For the second question, we will consider two limiting cases where $h(W_{max})$ can be simplified: i) large m/W_{rup} and ii) $m/W_{rup} = 0$.

3.2 Finite element simulations

We follow the approach of Zhang et al.[28] and build a finite element (FE) model in ABAQUS (v6.14, Simulia, Providence, RI). Briefly, as shown in Fig.4a, a crack is introduced into a plane stress pure-shear sample (dimensions: width L_0 = 480mm, height $2H_0$= 60mm, crack length a = 120mm). The bulk material behavior is implemented by combining the neo-Hookean model and the modified Ogden-Roxburgh model, both of which are built in ABAQUS. To allow comparison with Zhang et al.[28], we set μ=10kPa for the shear modulus and r=2, β=0.1 for the Mullins effect (see eqs.(18) and (20)) unless specified otherwise. The parameter m is subjected to change. A layer of cohesive elements was introduced directly ahead of the crack tip to enable the simulation of crack propagation. The explicit dynamics solver in ABAQUS is used to accommodate the rapid unloading associated with crack propagation. We impose a triangular traction separation law for the cohesive zone. The area underneath the traction separation curve is the intrinsic toughness Γ_0, which is rigorously proved from eq.(7) following an approach in literature[27,41] (see Appendix 2 for details). According to Zhang et al.[28], the modeling results converge when K is sufficiently large, K being the stiffness of the cohesive element prior to rupture (see Fig.4a). Therefore, we fix K/S_{max} at 200mm^{-1} and use different values for the maximum stress S_{max}. We interpret S_{max} as the maximum nominal tensile stress that can be achieved under uniaxial tension, beyond which rupture occurs. Following Zhang et al.[28], S_{max} can be related to W_{rup} using the following equation (see Appendix 3):

$$W_{rup} \approx S_{\max}^2 / 2\mu \ . \tag{35}$$

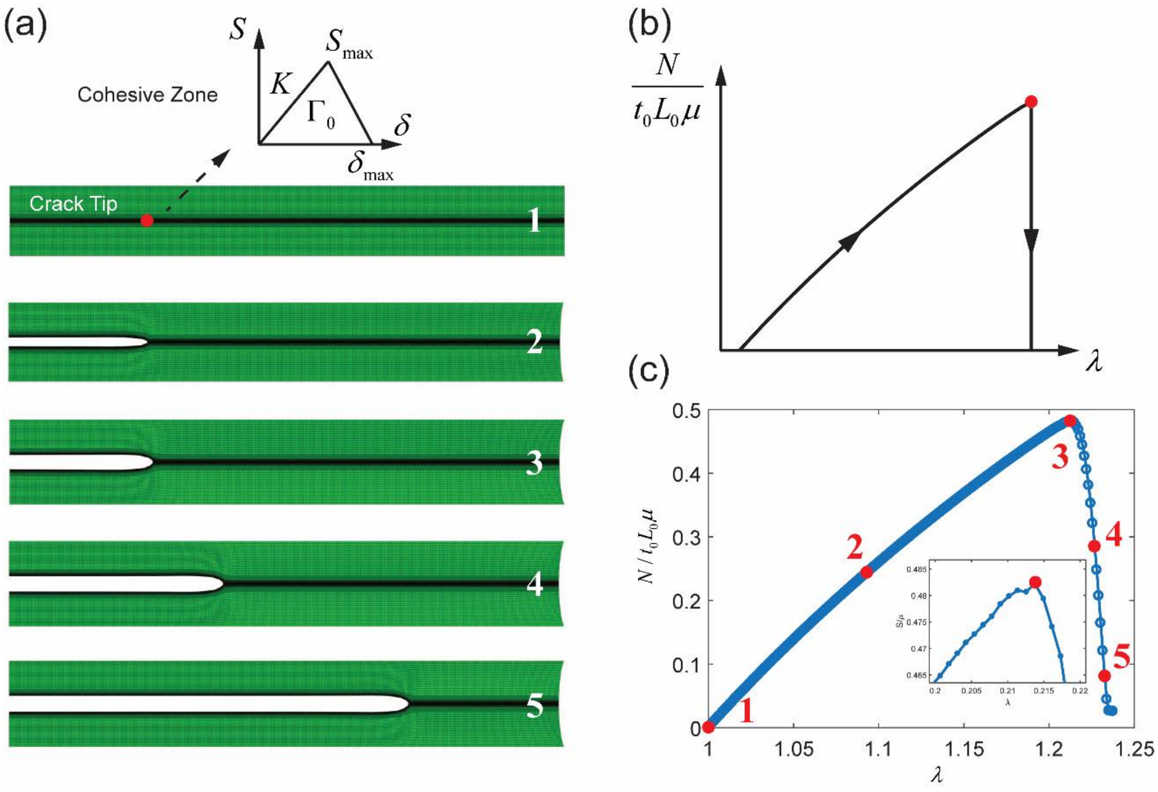

Figure 4 (a) Snapshots of crack propagation under the pure shear condition in FE simulation. The inset shows the cohesive zone model placed along the projected crack path. (b) Theoretical curve of the normalized force N versus applied stretch λ. Once the steady state stretch ratio λ_s is reached, the crack is expected to propagate catastrophically, which is represented by a sharp peak followed by an instantaneous drop in force. (c) A representative FE result (S_{max}/μ=4, Γ_0=30J/m^2, m/W_{rup}=0.05). The inset shows a zoomed view around the peak force. The points corresponding to the five snapshots in part (a) are also marked.

Our theory is based on the condition of steady state crack propagation under a fixed applied stretch λ_s. However, it is difficult to reproduce this scenario in simulation since the stretch λ_s needed to maintain steady state is not known a-priori. Instead, we continuously increase the displacement load and plot the applied force N versus applied stretch λ. Since the models for bulk material and cohesive zone are both rate independent, in principle the crack would propagate catastrophically once λ_s is achieved, leading to a sharp peak in the normalized N versus λ curve as schematically shown in Fig.4b. Motivated by this argument, we extract the λ at the maximum applied force from the FE results as the steady state stretch λ_s, and evaluate the total toughness Γ using $\Gamma=2H_0W_{far}(\lambda_s)$. This approach was also adopted in Zhang et al.[28]. We note that the FE result (see Fig.4c) does not exhibit an instantaneous drop after the peak force. This is because the simulations are based on the explicit dynamic solver of ABAQUS, and inertial effects prevent the crack propagation velocity from being infinite. In addition, oscillations associated with the dynamic solver may also bring slight uncertainties when identifying the location of peak force (see inset of Fig.4c). Given the importance of the N versus λ curve, we have performed a number of convergence tests to ensure the results are independent of mesh and simulation parameters, which are summarized in Appendix 3.

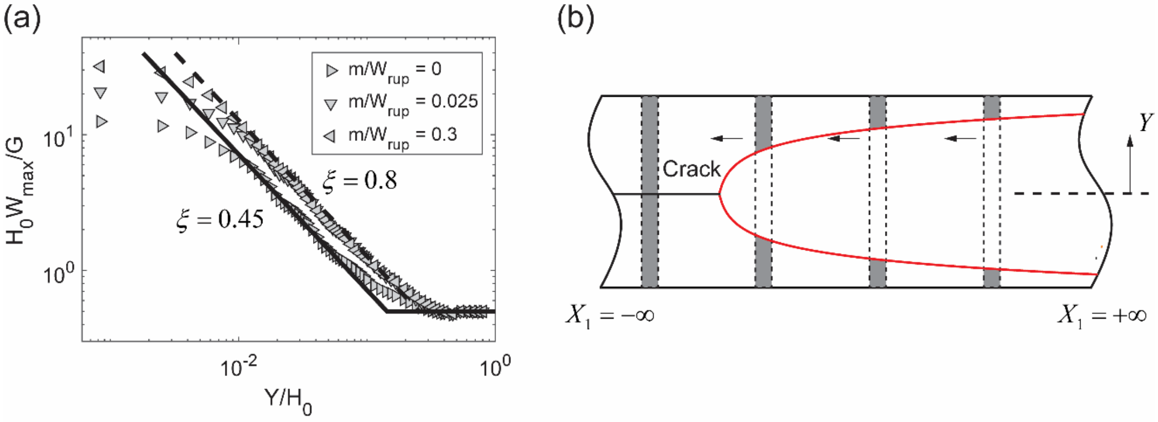

Figure 5 (a) Log-log plot of normalized W_{max} versus normalized Y. The symbols represent results extracted from the FE simulations for S_{max}/μ =4, Γ_0=30J/m^2, and three different values m/W_{rup}=0, 0.025, and 0.3. The lines are given by eq.(36) with an adjustable parameter ξ. (b) Evolution of the unloading zone as the vertical strip is moved from the right to the left. The red curve is plotted by extracting the location where W_{max} is achieved for a particular Y from an FE simulation, i.e. the case of m/W_{rup}= 0.3 in part (a). This curve illustrates how the unloading zone evolves as the vertical strip is translated to the left.

In Fig.5a, we plot $W_{max}(Y)$ during crack propagation from the FE results of three different cases. The theoretical picture sketched in Fig.3 captures the qualitative trend. However, to achieve quantitative agreement, a correction factor ξ ($0<\xi\leq 1$) is needed, i.e.,

$$W_{\max}\left(Y\right)=\begin{cases}\xi G/\left(2\pi Y\right) & Y_{coh}\leq Y\leq \xi H_0/\pi \\ G/\left(2H_0\right) & \xi H_0/\pi\leq Y\leq H_0\end{cases}. \tag{36}$$

To understand the physical origin of ξ, we plot in Fig.5b the boundary formed by the coordinates X_1 and Y at which the W_{max} is achieved using results of an FE simulation. This boundary illustrates how the unloading region evolves as a vertical strip is translated from X_1= +∞ to X_1= −∞. The $W_{max}(Y)$ in Fig.3 was derived for the elastic neo-Hookean solid. When hysteresis is introduced, the material in the unloading region is softer than the elastic counterpart, and thus is subjected to a larger stretch. Since the total stretch of the vertical strip is fixed at λ_s, the material points within the loading region (between the dashed lines in Fig.5b) experience a smaller stretch, which reduces W_{max}. With this correction, eq.(34) becomes

$$\frac{G_D}{G}=\frac{\xi}{\pi}\int_{G/(2H_0)}^{W_{rup}} h\left(W_{\max}\right)\frac{dW_{\max}}{W_{\max}}+\left(1-\frac{\xi}{\pi}\right)h\left(\frac{G}{2H_0}\right) . \tag{37}$$

Note that the correction factor ξ is not a constant but may vary as the bulk dissipation parameters change. Next we first use eq.(37) to derive solutions of G_D/G (or Γ_D/Γ) for two limiting cases, followed by the discussion about intermediate cases.

3.3 Limiting case I: localized dissipation (large m/W_{rup})

To motivate this limit, we plot the hysteresis ratio h versus $\phi=W_{max}/W_{rup}$ ($0\leq\phi\leq1$) in Fig.6a for four different values of m/W_{rup}. It can be seen that h decreases with m/W_{rup}. Specifically, in the extreme case of $m/W_{rup}=10$, h is less than 0.001 for $\phi\leq 0.0195$, indicating that the material is close to being elastic. Dissipation, if any, is limited to a small region near the crack tip. To better visualize this effect, we use the scaling relation $W_{max}\sim 1/Y$ (see eq.(36)) and plot h versus $Y/Y_{coh}=1/\phi$ in Fig.6b. For the case of $m/W_{rup}=10$, h rapidly decays to 0.001 when Y/Y_{coh} exceeds 50. Note that Y_{coh} represents the length scale of the cohesive zone and is by orders of magnitude smaller than H_0. Therefore, physically the limit of large m/W_{rup} corresponds to localized dissipation around the crack tip. Since h is small, we anticipate that the function $W_{max}(Y)$ based on the elastic crack tip solution to hold, which allows us to set $\xi=1$ and neglect the second term in eq.(37) accounting for the dissipation within $H_0/\pi\leq Y\leq H_0$. In addition, since $W_{max}\leq W_{rup}$, m/W_{max} is also large, and we can simplify eq.(25) by expanding the error function and exponential function into series and keeping only the first order terms, which gives

$$h\left(W_{\max}\right)\approx\frac{1}{r\sqrt{\pi}}\frac{1}{\beta+m/W_{\max}} . \tag{38}$$

Using these approximations and the change of variable $\phi=W_{max}/W_{rup}$, we can rewrite eq.(37) as

$$\frac{G_D}{G}\approx\frac{1}{r\pi^{3/2}}\int_{G/(2W_{rup}H_0)}^{1}\frac{1}{\beta\phi+m/W_{rup}}d\phi\approx\frac{1}{r\pi^{3/2}}\frac{W_{rup}}{m}\left(1-\frac{\pi Y_{coh}}{H_0}\right), \tag{39}$$

where we have used the definition $Y_{coh}=G/(2\pi W_{rup})$ to simplify the lower limit of the integral. Recognizing that $Y_{coh} << H_0$, we further simplify eq.(39) to

$$\frac{G_D}{G} = \frac{\Gamma_D}{\Gamma} \approx \frac{1}{r\pi^{3/2}} \frac{W_{rup}}{m} \quad . \tag{40}$$

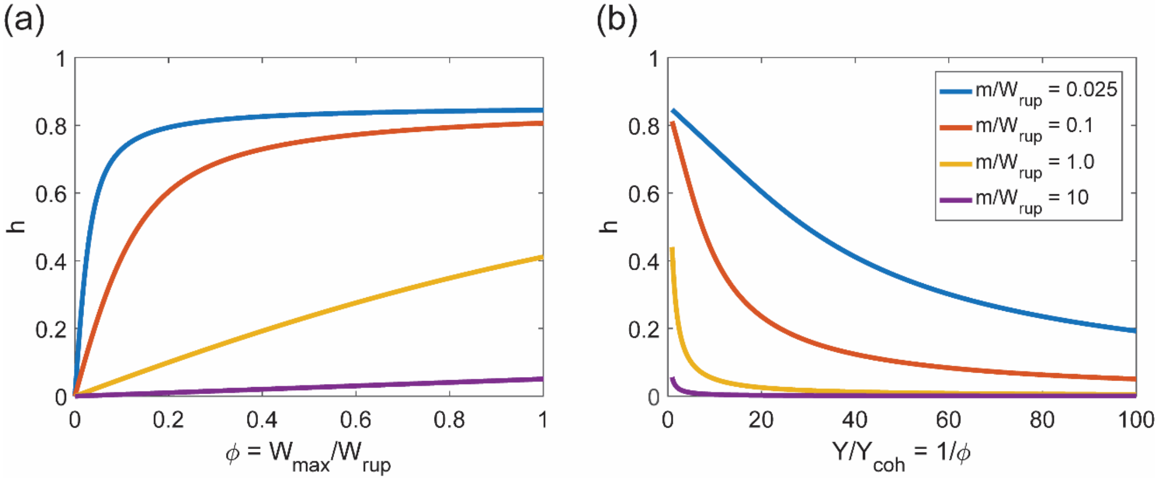

Figure 6 Hysteresis ratio h versus (a) the normalized nominal strain energy density $\phi = W_{max}/W_{rup}$, and (b) the normalized vertical coordinate Y/Y_{coh}, which is equal to $1/\phi$ due to the scaling $W_{max}{\sim}1/Y$. These curves are plotted using eq.(25) with r =1.1, β=0.1 and four different values of m/W_{rup} (0.025, 0.1, 1, 10).

To better visualize the physical picture of this limiting case, here we introduce a length scale Y_D to describe the dissipation zone size. Specifically, in light of eq.(26) Y_D defines a cut-off length such that G_D only comes from the region $-Y_D \leq Y \leq Y_D$ ($Y_D \leq H_0$) outside which U =0. However, according to the modified Ogden-Roxburgh model, U is non-zero for the entire region of $-H_0 \leq Y \leq H_0$, which requires us to relax the definition of Y_D: the majority of G_D, rather than all of G_D, is contributed by the region $-Y_D \leq Y \leq Y_D$. This definition of Y_D is associated with a custom defined threshold of G_D (e.g. 95%), which needs not be specified for the scaling considerations here. Motivated by eq.(36), we use the scaling relation $W_{max}(Y) \sim G/Y$ that is valid near the crack tip and obtain that $Y_D \sim G/W_c$ where W_c is a threshold of W_{max} that sets the boundary of the dissipation zone. As discussed above, dissipation is localized in a small region around the crack tip for the limiting case of $m/W_{rup} >> 1$, which implies that W_c is on the same order as W_{rup}. As a result, $Y_D \sim G/W_{rup} \sim Y_{coh}$, meaning that the dissipation zone size is comparable to the cohesive zone size, which is reminiscent of the "small scale yielding" condition in elastic-plastic fracture mechanics.

Zhang et al.[28] developed the following scaling relation

$$\frac{\Gamma_D}{\Gamma}=1-\frac{\Gamma_0}{\Gamma}=\alpha h_{rup} \text{ or } \Gamma=\frac{\Gamma_0}{1-\alpha h_{rup}}, \tag{41}$$

where h_{rup} is the hysteresis ratio at $W_{max} = W_{rup}$ and α is a numerical factor determined by fitting finite element results where β was fixed at 0.1:

$$\alpha=0.33+\frac{0.034}{m/W_{rup}+0.045}\ . \tag{42}$$

To facilitate comparison with Zhang et al.[28], we cast eq. (40) into the following form

$$\frac{\Gamma_D}{\Gamma}\approx\frac{1}{\pi}\left(1+\frac{\beta}{m/W_{rup}}\right)h_{rup}\quad \text{, where } h_{rup}=h\left(W_{rup}\right)\approx\frac{1}{r\sqrt{\pi}}\frac{1}{\beta+m/W_{rup}}. \tag{43}$$

Therefore, our analytical model suggests that when $\beta = 0.1$, the factor α is given by

$$\alpha\approx\frac{1}{\pi}+\frac{\beta/\pi}{m/W_{rup}}=0.32+\frac{0.032}{m/W_{rup}} \quad \text{for large } m/W_{rup}. \tag{44}$$

This analytical result agrees very well with eq.(42) given in Zhang et al.[28] in the limit of large m/W_{rup}. It is also worth mentioning that in this limit of large m/W_{rup}, α and Γ are independent of the fracture sample size H_0 since the dissipation is localized.

3.4 Limiting case II: constant hysteresis ratio (*m* =0)

In this case, we set $m = 0$, which implies that the hysteresis ratio h becomes independent of W_{max}, i.e.,

$$h\left(m=0\right)\equiv h_0=\frac{1}{r}\left[erf\left(\frac{1}{\beta}\right)+\frac{\beta}{\sqrt{\pi}}\left(e^{-1/\beta^2}-1\right)\right], \tag{45}$$

where h_0 is a constant for fixed values of r and β. Therefore, eq.(37) can be simplified to

$$\frac{G_D}{G}=\left[\frac{\xi}{\pi}\ln\frac{2H_0W_{rup}}{G}+\left(1-\frac{\xi}{\pi}\right)\right]h_0\ . \tag{46}$$

By setting $G_0=\Gamma_0$, $G_D=\Gamma_D$ and $G=\Gamma$, we can write eq.(46) into the following form:

$$\frac{\Gamma_0}{\Gamma}+\frac{\xi h_0}{\pi}\ln\frac{\Gamma_0}{\Gamma}=1-\frac{\xi h_0}{\pi}\ln\frac{2H_0W_{rup}}{\Gamma_0}-\left(1-\frac{\xi}{\pi}\right)h_0\ . \tag{47}$$

This equation allows us to solve for the ratio Γ/Γ_0 with given Γ_0 and h_0. Interestingly, the solution depends on a dimensionless parameter: $\chi = 2H_0W_{rup}/\Gamma_0$. This parameter reflects the ratio between the cohesive zone length scale and the sample height. To see that, we use eq.(35) and set $\Gamma_0 = S_{max}\delta_{max}/2$, where $\delta_{\max}$ is the maximum separation of the cohesive zone, which gives

$$\chi=\frac{2H_0W_{rup}}{\Gamma_0}=\frac{2S_{\max}}{\mu}\frac{H_0}{\delta_{\max}}\ . \tag{48}$$

Since $H_0 >> \delta_{max}$, we expect $\chi >>1$. In FE simulations, we can tune S_{max} and δ_{max} separately to alter χ. In Fig.7a, we plot the FE results (symbols) of Γ/Γ_0 versus χ for different combinations of S_{max} and δ_{max}. The data collapse onto a master curve. We also plot the predictions of eq.(47) in Fig.7a. If the correction factor ξ is set to be 1, our theory significantly overestimates the Γ/Γ_0. By plotting the distributions $W_{max}(Y)$ for a few representative cases in Fig.7b, we find that ξ ranges from 0.35 to 0.45. A much better agreement between the prediction of eq.(47) and FE results is obtained when ξ =0.35 is incorporated. We also notice that the FE results exhibit larger scattering for smaller χ. This is attributed to the fact that a smaller χ implies a larger δ_{max} which represents a wider cohesive zone. This may cause deviations from the assumed crack tip field in eq.(36). As a result, the FE data for smaller χ show larger scattering around the master curve predicted by eq.(47) than those for larger χ.

Interestingly, our analytical model and FE results both suggest that Γ depends on the sample size H_0 and the cohesive parameters S_{max} and δ_{max} through χ. Physically since the hysteresis ratio h is constant for m =0, dissipation occurring even far away from the crack tip is also important. Although the area of hysteresis loop U decreases as one moves away from the crack tip, this decay is compensated by the large volume of materials in the far field. Also, the amount of dissipation depends on the deformation field which is highly coupled to the cohesive zone. This is quite different from the "small-scale yielding" limit for large m/W_{rup} where Γ is independent of sample size H_0.

Indeed, the dissipation zone size $Y_D \sim G/W_c$ can be estimated by recognizing that the threshold W_c is on the same order of W_{far}, since dissipation over the entire sample needs to be taken into account. Therefore, $Y_D \sim G/W_{far} \sim H_0$, meaning that the dissipation zone size is on the same order of the sample height. Note that the scaling relation $Y_D \sim G/W_c$ is only valid for $|Y| \le \xi H_0/\pi$, but this does not affect the scaling argument above. Lastly, we note that in Zhang et al.[28], Γ/Γ_0 at m =0 is given by a constant: $1/(1-\alpha_0 h_0)$, where α_0 =1.0856 (see eq.(42)). The value of Γ/Γ_0 given by the empirical formula of Zhang et al.[28] is also plotted in Fig.7a for comparison (see the horizontal dotted line).

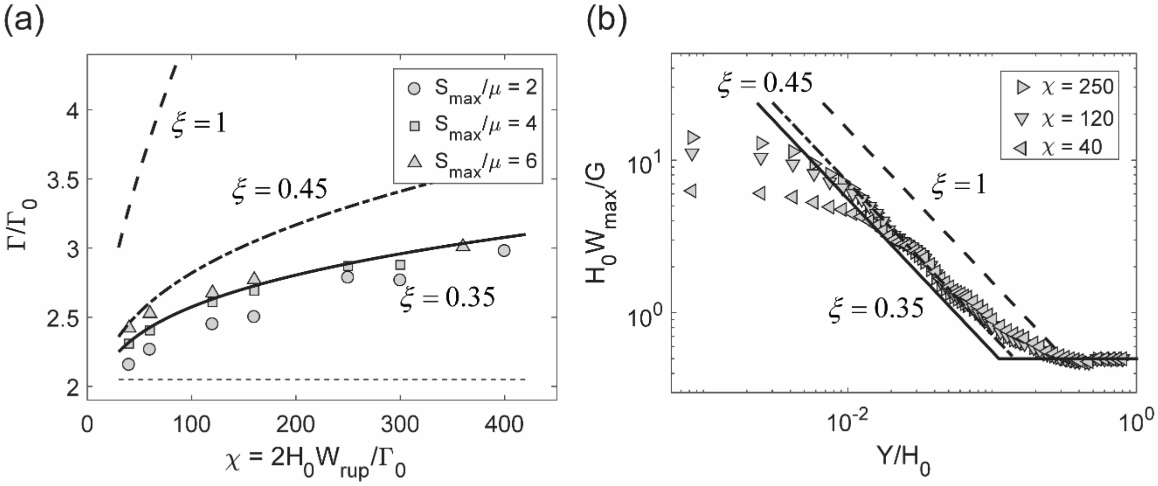

Figure 7 (a) Toughness enhancement Γ/Γ_0 versus the dimensionless parameter χ in the limit of m =0. The symbols are given by FE result and the curves are predictions based on eq.(47) with three different values of ξ. The horizontal dotted line is the prediction of the formula in Zhang et al.[28] (see eq.(41) and (42)). (b) Log-log plot of normalized W_{max} and normalized Y. The symbols are extracted from FE data where S_{max}/μ =4 and χ= 250, 120, 40, and the lines are fits based on eq.(36)) with ξ being the only adjustable parameter.

3.5 Intermediate cases

For intermediate values of m/W_{rup}, we would need to solve eq.(37) for Γ (with $G_0 = \Gamma_0$) where analytical solutions are difficult to obtain. Moreover, the correction factor ξ is not known unless FE simulations are carried out. To circumvent these difficulties, we draw inspirations from Zhang et al.[28] and construct the following equation

$$\frac{\Gamma_D}{\Gamma} = 1 - \frac{\Gamma_0}{\Gamma} = \alpha h_{rup} = \underbrace{\frac{1}{\pi}\left(1 + \frac{\beta}{m / W_{rup} + \zeta}\right)}_{\alpha} h_{rup} \ . \tag{49}$$

Equation (49) reduces to eq.(44) in the limit of large m/W_{rup}. An additional parameter ζ is introduced so that eq.(49) would match the solution of eq.(47) when m/W_{rup}=0:

$$\zeta = \frac{\beta}{\frac{\pi}{h_0}\left(1 - \left.\frac{\Gamma_0}{\Gamma}\right|_{m=0}\right) - 1} \ . \tag{50}$$

Since the value of Γ_0/Γ at m=0 depends on the dimensionless parameter χ, we use the eq.(47) (with ξ=0.35 and χ ranging from 10 to 400) and eq.(50) to determine a range of ζ: 0.0286~0.0425. With this range of ζ, the numerical factor α predicted by eq.(49) is shown as the shaded area in Fig.8. The empirical formula of Zhang et al.[28] (see eq.(42)) and the limiting case eq.(44) are also plotted for comparison. These curves deviate from each other at small m/W_{rup} but start to converge when m/W_{rup} exceeds 0.15.

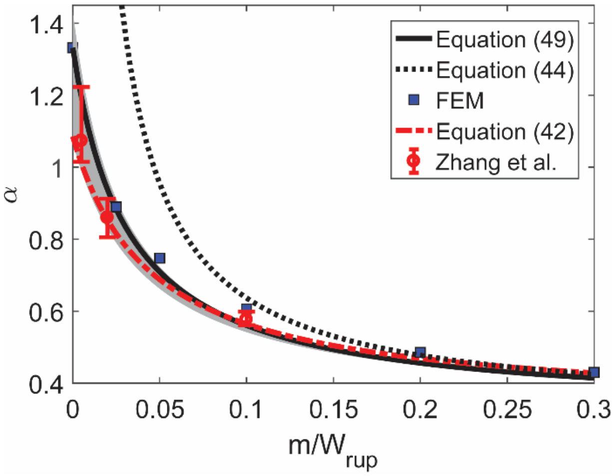

Figure 8 Dimensionless factor α (related to toughness enhancement) versus m/W_{rup} (related to bulk hysteresis). The shaded region are given by eq.(49) with ζ ranging from 0.0286 to 0.0425. The square symbols represent our FE data and the solid line is the corresponding model prediction. The circular symbols (red) are data points extracted from the FE results of Zhang et al.[28], where the circle represents the mean value of α for a given m/W_{rup} and the error bar illustrates the range of scattering. The empirical formula of Zhang et al.[28] (red dashed line) and the analytical solution in the limit of large m/W_{rup} (dotted line) are also plotted for comparison.

To test the predictive power of eq.(49) for intermediate m/W_{rup}, we plotted the factor α extracted from finite element results with $S_{max}/\mu=4$, $\delta_{max}/H_0=0.05$ and varying m. This set of parameters are chosen to ensure a fixed χ = 160, which corresponds to ζ =0.0314. As shown in Fig.8, the FE results (square symbols) agree well with eq.(49) (solid line). Furthermore, we extract the FE data for Γ/Γ_0 in Zhang et al.[28] (see their Fig.3b) and use eq.(41) to calculate the corresponding values of α. It turns out that there is a considerable scattering when m/W_{rup} is small (see Fig.8). This scattering can be explained by our model. The FE parameters in Zhang et al.[28] correspond to a range of χ (80~300), and theoretically speaking the data of α for different χ should not collapse exactly to a master curve, as manifested in the shaded area in Fig.8. This is consistent with the observation that eq.(41) cannot precisely fit all the FE data points in Fig.3b of Zhang et al.[28] with a single value of α. This phenomenon highlights the importance of the detailed fracture behaviors at the crack tip, which are modeled by the cohesive zone parameters appearing in χ, in case of large dissipation zone.

4. Effect of pre-stretch

According to the Ogden-Roxburgh model for Mullins effect (see eqs.(19) and (20)), hysteresis occurs only during the first loading-unloading cycle. The material behaves elastically upon reloading as long as W does not exceed the maximum value of W experienced in the loading history. This feature implies that pre-stretch can reduce the toughness Γ by decreasing the bulk dissipation in the fracture sample. The effect of pre-stretch on Γ has been experimentally demonstrated in Zhang et al.[28]. In such experiments, two identical uncracked pure shear samples would need to be first subjected to a pre-stretch ratio λ_{pre}. After that an edge crack would be introduced into one of pre-stretched samples for measuring Γ using eq.(21) where the function W_{far} can be determined using the other uncracked pre-stretched sample[12,19]. Zhang et al.[28] showed that the toughness Γ decreases with λ_{pre} and reaches a plateau for sufficiently large λ_{pre}. Despite the experimental finding, the effect of pre-stretch has not been fully understood at the theoretical level. Here we present an analytical model for the effect of pre-stretch.

4.1 Analytical model

We denote the nominal strain energy density associated with the pre-stretch by W_{pre}. Since the principal stretch ratios are λ_1=1, λ_2=λ_{pre}, λ_3=1/ λ_{pre} under pure shear, W_{pre} is given by:

$$W_{pre} = \frac{\mu}{2}\left(\lambda_{pre}^{2} + \lambda_{pre}^{-2} - 2\right). \tag{51}$$

The pre-stretch brings two changes to our energy balance model. First, recall that the dissipative energy release rate G_D is the integral of U along the vertical strip in the pure shear sample (see Fig.9a and eq.(26)), where U is the energy dissipation per unit reference volume and is a function of the maximum deformation, represented by W_{max}, experienced by a material point. Because of the pre-stretch, U is no longer equal to $h(W_{max})$ W_{max}. Instead, U should be

$$U = \begin{cases} 0 & W_{\max} \le W_{pre} \\ h\left(W_{\max}\right)W_{\max} - h\left(W_{pre}\right)W_{pre} & W_{\max} > W_{pre} \end{cases}, \tag{52}$$

where the hysteresis ratio h is given in eq.(25). Second, the loading branch after pre-stretch (solid line in Fig.9b) deviates from the original one (dashed line in Fig.9b). Therefore, when evaluating the total energy release rate G using eq.(21), we need to replace W_{far} by the work per unit volume required to achieve the global stretch λ_s for steady-state crack propagation. This work per unit volume, denoted by $\tilde{W}_{far}$, can be calculated by

$$\tilde{W}_{far} = \begin{cases} \int_{0}^{W_{far}} \eta dW = W_{far} - \frac{1}{r}\int_{0}^{W_{far}} erf\left(\frac{W_{pre} - W}{m + \beta W_{pre}}\right) dW & W_{far} \le W_{pre} \\ W_{far} - h\left(W_{pre}\right)W_{pre} & W_{far} > W_{pre} \end{cases}, \tag{53}$$

where $W_{far} = \mu(\lambda_s^2 + \lambda_s^{-2} - 2)/2$.

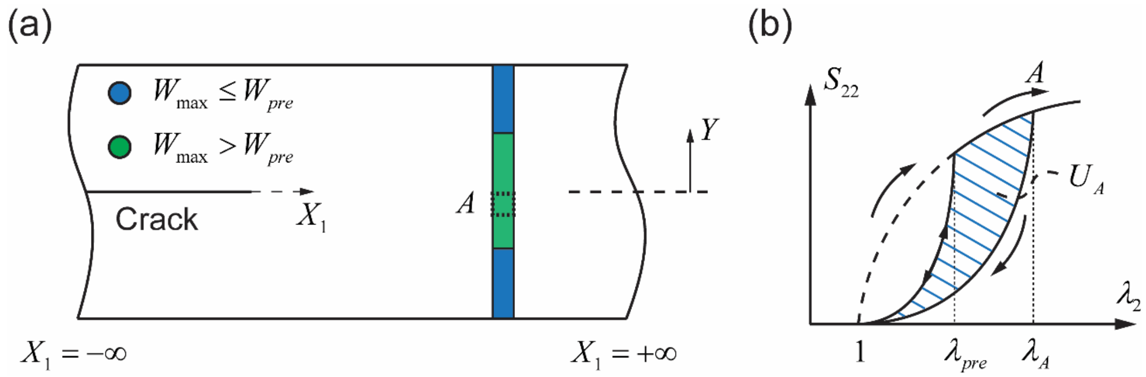

Figure 9. (a) The vertical strip used to calculate G_D is divided into two regions: $W_{max} \leq W_{pre}$ (blue) and $W_{max} > W_{pre}$ (green). (b) Due to the pre-stretch, the initial loading curve of a point A changes from the dashed line to the solid line (softened) when $\lambda_2 < \lambda_{pre}$. Once $\lambda_2 \geq \lambda_{pre}$, the initial loading curve is recovered. Therefore, the hysteresis U_A is reduced due to the pre-stretch.

Our strategy to account for the effect of pre-stretch is to subtract the energy dissipation consumed during pre-stretch from G_D. As shown in Fig.9a, the vertical strip used to calculate G_D can be divided into two regions: (i) elastic region where $W_{max} \leq W_{pre}$ (blue) and (ii) dissipative region where $W_{max} > W_{pre}$ (green). Dissipation only occurs in Region (ii) since U =0 in Region (i). The size of each region depends on the relative comparison between the pre-stretch λ_{pre} (or equivalently W_{pre}) and the stretch λ_s (or equivalently W_{far}) to maintain steady-state crack propagation in the same sample without pre-stretch. This leads to three cases to be discussed below. To visualize the three cases, we plot the function $W_{max}(Y)$ in Fig.10a according to eq.(36) assuming no pre-stretch. Note that Fig.10a is in log-log scale, and we have switched the W_{max} and Y axes in comparison to Fig.3b so that the Y-axis is aligned with the vertical strip. Also, the cohesive zone is not shown in Fig.10a. Recall that the function $W_{max}(Y)$ plotted in Fig.10a was obtained by combining the solution for neo-Hookean model (see Fig.3b) and a correction factor ξ based on the finite element data (see Fig.5a). As seen in Fig.10a, the main difference between the three cases is the relative extent of the elastic region (blue) and dissipative region (green), which depends on the level of pre-stretch.

Case I: Small pre-stretch

In this case we assume $W_{pre} < W_{far}$ (or $\lambda_{pre} < \lambda_s$), which implies the entire strip is covered by the dissipative region (see Fig.10a). According to eq.(52), we need to subtract the same amount, i.e. $h_{pre}W_{pre}$, from U at every material point along the vertical strip. In principle pre-stretch may also affect the crack tip deformation field since it alters the stress/strain relation during loading branch. However, as a first order approximation, we neglect this effect and still apply the deformation field assumed in Section 3. As a result, the dissipative energy release rate G_D^* with pre-stretch is

$$G_D^* = G_D - 2\int_0^{H_0} h(W_{pre})W_{pre}dY \ , \tag{54}$$

where G_D is the counterpart of G_D^* under no pre-stretch. To derive the toughness Γ^* under pre-stretch, we set $G_D^* = \Gamma_D^* = \Gamma^* - \Gamma_0$ and use eq.(49) to replace G_D by Γ_D, which gives

$$\Gamma^* = \frac{\Gamma_0}{1-\alpha h_{rup}} - 2H_0 h(W_{pre})W_{pre}, \tag{55}$$

where α is the dimensionless factor appearing in eq.(49) for the no pre-stretch case.

Case II: Intermediate pre-stretch

In this case we assume $W_{pre} >\sim W_{far}$ (or $\lambda_{pre} >\sim \lambda_s$), which implies that the elastic region approximately covers a range of Y where $W_{max} = W_{far}$ (see Fig.10a). No dissipation would occur in the elastic region. To estimate G_D^*, we first assume the scaling relation that $W_{max} = \xi G/(2\pi Y)$ is still valid in the dissipative region. By following similar derivation for eq.(37), we obtain

$$\frac{G_D^*}{G^*} = \frac{\xi}{\pi}\int_{W_{pre}}^{W_{rup}} h^*\left(W_{\max}\right)\frac{dW_{\max}}{W_{\max}}, \tag{56}$$

where hysteresis ratio h^* under pre-stretch is refined as:

$$h^*\left(W_{\max}\right) = \frac{U}{W_{\max}} = \begin{cases} 0 & W_{\max} \le W_{pre} \\ h\left(W_{\max}\right) - \dfrac{h\left(W_{pre}\right)W_{pre}}{W_{\max}} & W_{\max} > W_{pre} \end{cases} . \tag{57}$$

Substituting eq.(57) into eq.(56) and applying the change of variable $\phi = W_{max}/W_{rup}$, eq.(56) becomes

$$\frac{G_D^*}{G^*} = \frac{\xi}{\pi} \int_{W_{pre}}^{W_{rup}} h\left(W_{\max}\right) \frac{dW_{\max}}{W_{\max}} - \frac{\xi}{\pi} h\left(W_{pre}\right)\left(1-\phi_0\right), \tag{58}$$

where $\phi_0 = W_{pre}/W_{rup}$. The first term on the right hand side of eq.(58) represents the dissipation as if there were no pre-stretch, whereas the second term accounts for the reduced dissipation due to pre-stretch. However, this equation is difficult to use since the correction factor ξ is not known. Unlike Section 3 where we focus on demonstrating the utility of energy method for calculating G_D and thus used the FE data to determine ξ (see Fig.7a for example), here our goal is to obtain analytical equations to predict the dependence of G_D on pre-stretch. Therefore, two additional approximations are used to simplify eq.(58) and allow the prediction of Γ^*, as described below.

First, since W_{pre} is comparable to W_{far}, we recognize that the integral term in eq.(58) is approximately equal to the integral term in eq.(37) (note that $G/2H_0$ is equal to W_{far}). Therefore, we make an approximation to replace the integral in eq.(58) by the ratio G_D/G under no pre-stretch. Effectively we neglected the second term in eq.(37). This is based on the assumption that most of the dissipation comes from the region with strong stress concentration where $W_{max} \sim 1/Y$, represented by the integral term in eq.(37). Furthermore, using eq.(49) we find $G_D/G = \alpha h_{\mathrm{rup}}$. Therefore,

$$\frac{G_D^*}{G^*} = \alpha h_{rup} - \frac{\xi}{\pi} h\left(W_{pre}\right)\left(1-\phi_0\right). \tag{59}$$

This approximation tends to overestimate G_D^*/G^*. Second, we neglect effect of the correction factor ξ ($0 < \xi \leq 1$) and make the approximation that $\xi = 1$, which implies

$$\frac{G_D^*}{G^*} = \alpha h_{rup} - \frac{1}{\pi} h\left(W_{pre}\right)\left(1-\phi_0\right). \tag{60}$$

This approximation tends to underestimate G_D^*/G^*. Therefore, errors due to the two approximations may cancel each other, at least partially. Finally by using $G_D^*/G^* = \Gamma_D^*/\Gamma^*$, we can get:

$$\Gamma^* = \frac{\Gamma_0}{1-\alpha h_{rup} + \frac{1}{\pi} h\left(W_{pre}\right)\left(1-\frac{W_{pre}}{W_{rup}}\right)} . \tag{61}$$

It is difficult to theoretically estimate the errors due to the two approximations made above. Instead, in Section 4.2 we will show that eq.(61) is in good agreement with the FE results, which serves as a justification for these two approximations.

Case III: Large pre-stretch

In this case we assume $W_{pre} >> W_{far}$ (or $\lambda_{pre} >> \lambda_s$). Similar to Case II, we can derive eq.(58) for estimating G_D^*. However, unlike Case II, here dissipation is confined to a small region around crack tip (see Fig.10a). Outside the dissipative region, the material behaves as an elastic neo-Hookean solid, but with a reduced modulus due to pre-stretch. Therefore, we recover the scenario of localized dissipation, and hypothesize that the crack tip field based on elastic neo-Hookean solid is valid. In other words, ξ =1. As a result, eq.(58) becomes

$$\frac{G_D^*}{G^*} = \frac{1}{\pi}\int_{\phi_0}^{1} h\left(\phi W_{rup}\right)\frac{d\phi}{\phi} - \frac{1}{\pi} h\left(W_{pre}\right)\left(1-\phi_0\right), \tag{62}$$

where $\phi_0 = W_{pre}/W_{rup}$. Again, by using $G_D^*/G^* = \Gamma_D^*/\Gamma^*$, we can get:

$$\Gamma^* = \frac{\Gamma_0}{1-\frac{1}{\pi}\int_{\phi_0}^{1} h\left(\phi W_{rup}\right)\frac{d\phi}{\phi} + \frac{1}{\pi} h\left(W_{pre}\right)\left(1-\phi_0\right)} . \tag{63}$$

It should be noted that the scenario of localized dissipation is achieved through pre-stretch, which is applicable for all values of m/W_{rup}. In contrast, the special case of localized dissipation in Section 3.3 assumes zero pre-stretch and thus is only applicable when m/W_{rup} is large.

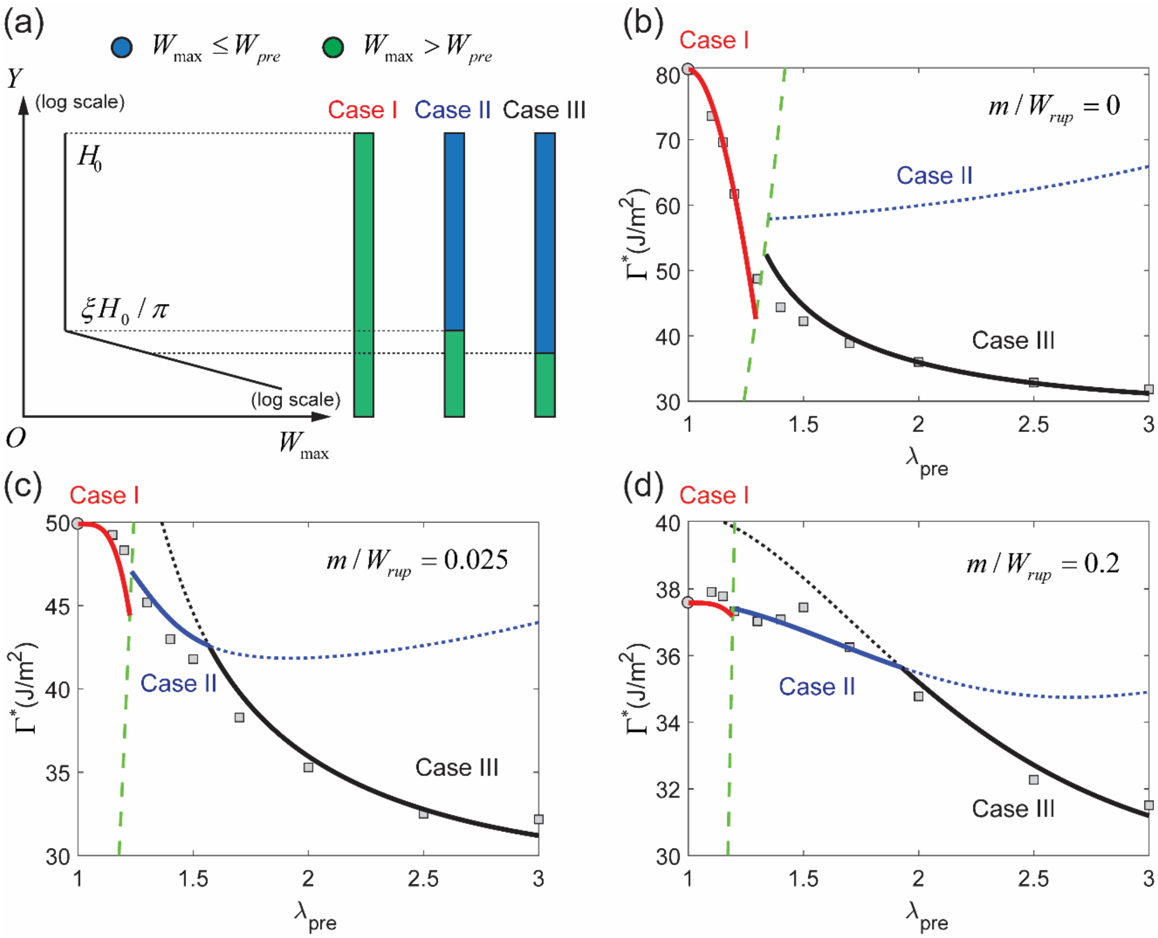

Figure 10 (a) Schematics of the three cases considered in our analytical model. The Y versus W_{max} plot is in log-log scale and is used to illustrate the difference between the three cases. (b-d) Comparison between predictions of our model and FE data (symbols) for fracture toughness Γ^* versus pre-stretch λ_{pre} for three values of m/W_{rup} =0, 0.025, 0.2.

4.2 Model validation

We perform a set of FE simulations with the same cohesive zone parameters with peak stress S_{max}/μ =4 and intrinsic toughness $\Gamma_0/\mu t_0$ = 3 where the shear modulus μ = 10kPa and thickness t_0 =1mm. This corresponds to W_{rup} = 80kJ/m^3 using eq.(35). The rest of the parameters are: sample height $2H_0$ =60mm and Mullins effect parameters r = 2 and β = 0.1. For each run, we first simulate the pre-stretch process by uniformly stretching an uncracked sample to λ_{pre} under the pure shear condition. After that, we introduce an edge crack and simulate the pure shear fracture test, determine the stretch ratio associated with the peak force, and interpret it as the λ_s for steady state crack propagation. The toughness Γ* is calculated using

$$\Gamma^* = 2H_0\tilde{W}_{far}\left(\lambda_1 = 1, \lambda_2 = \lambda_s, \lambda_3 = 1/\lambda_s\right) , \tag{64}$$

where $\tilde{W}_{far}$ is defined in eq.(53) and accounts for the softening due to pre-stretch. This procedure is repeated for different pre-stretches λ_{pre} to determine how Γ* decays with λ_{pre}.

The FE results are plotted in Fig.10b-d for three values of m/W_{rup} (0, 0.025, and 0.2). To plot the predictions of our analytical model, we note that the boundary between Case I and Case II&III is determined by the condition $W_{pre} = W_{far}$. By relating W_{far} to $\tilde{W}_{far}$ and Γ* through eqs. (53) and (64), we can rewrite this condition as:

$$\left[1 - h\left(W_{pre}\right)\right]W_{pre} = \tilde{W}_{far} = \frac{\Gamma^*}{2H_0} . \tag{65}$$

Since W_{pre} is a function of λ_{pre} as defined in eq.(51), we plot eq.(65) in Fig.10b-d as a green dashed curve. Above the curve, Case I is valid. Below this curve, either Case II or III is valid. The difference between Case II and III is whether the pre-stretch has significantly altered the crack tip deformation, which is difficult to be captured by an analytical relation. Therefore, we plot both cases and choose the one with lower Γ* (see solid lines). It should be emphasized that all the parameters involved in the analytical model can be directly calculated using parameters of the FE simulations. In particular, ideally we would use eq.(49) to predict the factor α at zero pre-stretch. However, as shown in Fig.8, there is a slight discrepancy between eq.(49) and corresponding FE results when m/W_{rup} exceeds 0.05. To focus on the effect of pre-stretch, we take the FE result of toughness Γ at zero pre-stretch and evaluate α using $\alpha = (1-\Gamma_0/\Gamma)/h_{rup}$. Excellent quantitative agreement between the model predictions and FE results can be seen in Fig.10b-c. As expected, Case I, II and III can capture the reduction in toughness Γ* at small, intermediate and large pre-stretch, respectively. The transition occurring near the boundary represented in eq.(65) is not smooth, which is due to the approximations used in the analytical model. It is interesting to note that as m/W_{rup} decreases, the region of validity for Case II decreases and eventually vanishes when m/W_{rup} =0.

Next we examine the experimental data in Zhang et al.[28] to see how well our analytical model can capture their data. Specifically, they tested the toughness of a polyacrylamide-alginate hydrogel[12] under different pre-stretch ratios, as shown in Fig.11 (symbols). To apply our model, we first describe how relevant parameters are selected. Pure shear extensional tests show that the loading branch of the curve can be described by a one-term Ogden model:

$$W_{pre} = \frac{2\mu}{\kappa^2}\left(\lambda_1^{\kappa} + \lambda_2^{\kappa} + \lambda_3^{\kappa} - 3\right) , \tag{66}$$

where μ = 10.81kPa and κ =1.879. Our model was based on the neo-Hookean model which can be recovered from eq.(66) by setting κ=2. For simplicity we will neglect this difference and directly apply our model to this hydrogel. By fitting the experimentally measured hysteresis ratio h with the modified Ogden-Roxburgh model, they determined that r =1.516, m = 4.274kJ/m^3 and β =0.1. The peak stress of cohesive zone S_{max} was taken to be the maximum stress recorded under the pure-shear extensional test and is S_{max} =80kPa. For the Odgen model, the approximate approach in eq.(35) to estimate W_{rup} is no longer applicable. Therefore, we use eq.(66) to estimate W_{rup}, and find W_{rup} =358.5kJ/m^3 and m/W_{rup} =0.012. The intrinsic toughness Γ_0 is taken to be the plateau value of Γ^* at large pre-stretch λ_{pre}, i.e. Γ_0=400 J/m^2 (see Fig.5c in Zhang et al.[28]). Lastly, with the sample height $2H_0$=20mm, we find $2H_0W_{rup}/\Gamma_0$ =17.93 in eq.(47). Assuming ξ =0.35 (see Fig.7a), eq.(47) allows us to get Γ_0/Γ =0.325, which further leads to ζ =0.0415 based on eq.(50). Finally, using eq.(49), we find α =0.9139 for m/W_{rup}=0.012, implying the toughness under zero pre-stretch is Γ=919J/m^2 which is about 10% lower than the experimental data (1063J/m^2).

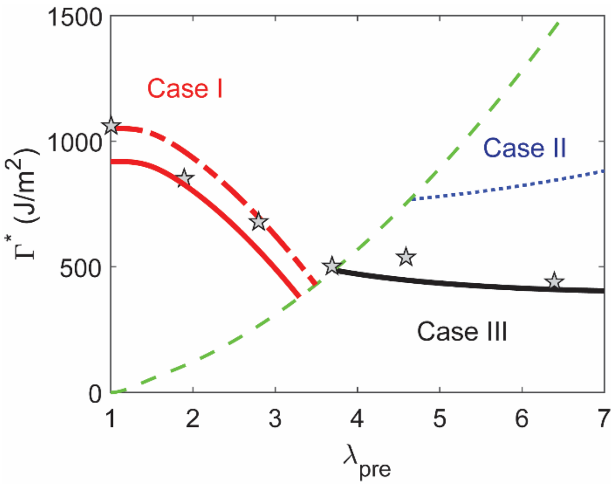

Figure 11 Comparison of the model predictions and experimental data on how the toughness Γ* depends on pre-stretch λ_{pre}. The experimental data (star symbols) are extracted from Zhang et al.[28]. From the experimental data, m/W_{rup} is found to be 0.012, and it turns out that Case II of the model does not exhibit a region of validity, similar to the case of m=0 in Fig.10b.

Now that all the parameters are determined, we plot the prediction of our analytical model in Fig.11. The model predictions agree with the experimental data reasonably well, given that there is no adjustable parameter in the model. In the range of λ_{pre} where Case I is applicable, our model underestimates Γ* in comparison to experimental data, which comes from the lower estimate of Γ for zero pre-stretch. This is not surprising since we have used eq.(36) with ξ=0.35 based on the neo-Hookean model to derive α, which may not be accurate for the Ogden model in eq.(66) even though κ is close to 2. However, our model does capture the relative trend of decaying Γ* with λ_{pre}. To illustrate this point, we use the experimental value of Γ (=1063J/m^2) at zero pre-stretch to find $\alpha = 1.0093$. The Case I based on this value of α (see eq.(55)) is shown in Fig.11 as the dashed line (red), and it gives a better agreement with experimental data.

5. Summary and Discussions

We presented a method to calculate the fracture toughness of a model soft dissipative material system, i.e., neo-Hookean solids with rate-independent hysteresis described by the Mullins effect. Based on energy balance, we first derived a general equation connecting the energy release rate to bulk hysteresis, and then applied it to steady-state crack propagation and the constitutive model of neo-Hookean solid with Mullins effect. By leveraging the solutions for crack tip deformation field in elastic neo-Hookean solids, we developed analytical expressions illustrating how toughness is enhanced by the bulk dissipation, and validated them using FE simulations. Using the same theoretical framework, we also derived an analytical model to quantitatively capture the reduction in fracture toughness due to pre-stretch, which agrees with FE results and literature experimental data well. Such analytical relations will serve as useful tools for predicting fracture behaviors in soft dissipative materials where the Mullins effect is dominant, e.g. filled elastomer[29], double network gel[11] and multi-network elastomer[14].

Using the modified Ogden-Roxburgh model as an example, we found that the dissipation zone size can be tuned by modifying the bulk hysteresis parameters. In particular, in the limit of $m/W_{rup} >>1$, the dissipation zone is localized near the crack tip and Γ is independent of the sample size H_0, reminiscent of the "small scale yielding" condition in elastic-plastic fracture. However, in the limit of $m=0$, we found that dissipation from the material far away from the crack tip cannot be neglected due to its large volume. In this case, the dissipation zone size Y_D is always comparable to H_0, and the scenario of "large scale yielding" is evoked. Theoretically speaking, the total toughness Γ becomes dependent on the sample size, although this dependence is rather weak as shown in Fig.7a. Nevertheless, the size dependent toughness Γ may pose a challenge to the characterization of fracture in soft materials with significant dissipation, e.g. viscoelastic elastomers[16,42] or tough hydrogels[12,13] with highly enhanced hysteresis and crack blunting.

A limitation of our version of the Ogden-Roxburgh model is that it leads to a negative dissipation rate during reloading after a loading-unloading cycle, which violates the second law of thermodynamics. A more physical approach[30,43–45] to capture the Mullins effect is to let the damage variable η in eq.(18) evolve during the loading branch ($\mathrm{d}\eta < 0$) and remain unchanged during unloading or reloading ($\mathrm{d}\eta = 0$), so that the dissipation rate is always non-negative. To illustrate how this type of model can be combined with our thermodynamic framework for crack propagation, we plot in Fig.12 the loading history of a material point as it is translated from $X_1 = +\infty$ to $X_1 = -\infty$ in the pure shear fracture specimen (see Fig.1a), schematically represented by the dominating stress and stretch components: S_{22} versus λ_2. Since $\mathrm{d}\eta = 0$ during unloading, the integral for the dissipation term U in eq.(23) only comes from the loading branch, starting at the global stretch λ_s and ending at the maximum stretch experienced by this point. Using integration by parts or a graphical method similar to that in Section 2.3 (see eq.(24) and associated discussions), one can show that U is represented by the gray shaded area in Fig.12, instead of the entire hysteresis loop. On the other hand, eq.(13) reduces to

$$G = 2H_0\psi\left(X_1 = +\infty\right) = 2H_0\underbrace{\eta\left(\lambda_2 = \lambda_s\right)W\left(\lambda_2 = \lambda_s\right)}_{\psi_s} , \tag{67}$$

where ψ_s is the free energy density far ahead of the crack tip (illustrated by the blue line shaded region in Fig.12). Following the thermodynamic framework, we obtain

$$G_D = G - G_0 = \int_{-H_0}^{H_0} U dY , \tag{68}$$

but the physical meaning of G and U are different from what we had in Section 2.3 in that here U is only given by part of the hysteresis loop and G is defined using the area underneath the unloading curve at λ_s (dashed line in Fig.12). To reconcile this difference, we note that in the literature[12,13,19,28] the global energy release rate is typically defined using the mechanical work required to achieve the global stretch λ_s rather than the free energy. According to this definition, the global energy release rate G^* is

$$G^* = 2H_0\left(\psi_s + U_s\right) = G + 2H_0U_s , \tag{69}$$

where U_s is area of the hysteresis loop associated with the global stretch λ_s. Combining eq.(68) and (69), we have

$$G_D^* = G^* - G_0 = 2H_0U_s + \int_{-H_0}^{H_0} U dY = \int_{-H_0}^{H_0} U^* dY , \tag{70}$$

where $U^* \equiv U + U_\mathrm{s}$ is the area of the entire hysteresis loop experienced by the material point (i.e., red line shaded region + gray shaded region in Fig.12). This definition of G^* and U^* are now consistent with those based on the Ogden-Roxburgh model (see Section 2.3). Physically G in eq.(67) represents the free energy that can be released by the vertical strip far ahead of the crack tip, while G^* in eq.(69) quantifies the work required to drive crack propagation. These two definitions are not in contradiction but rather complement each other. For example, G^* can describe a material's resistance to crack propagation, while G is better correlated with physical process of crack propagation as demonstrated in a recent experimental work[46].

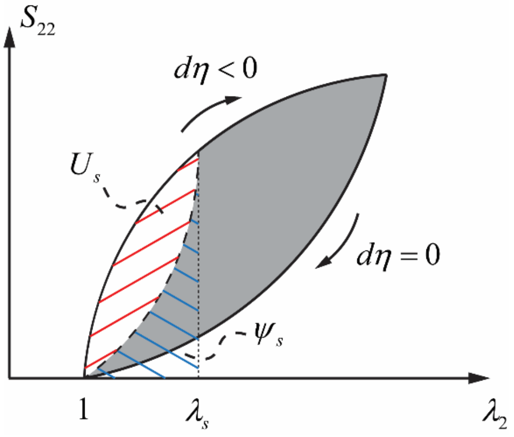

Figure 12 The loading history for a representative material point during steady state crack propagation in a pure shear fracture specimen. Unlike the material model assumed in Section 2.3, here dissipation occurs during the loading branch ($d\eta < 0$) but not the unloading branch ($d\eta = 0$).

From a theoretical perspective, our work demonstrated a general strategy to calculate the contribution to fracture toughness due to bulk dissipation, which relies on knowledge in two aspects: i) deformation and stress fields in the crack sample; ii) nonlinear constitutive relation for the bulk material. This strategy can be extended to more complex material systems. For example, a possible extension to account for the strain stiffening effect at very large stretches is to replace the neo-Hookean model by the generalized neo-Hookean (GNH) model:

$$W = \frac{\mu}{2b}\left\{\left[1+\frac{b}{n}\left(\sum_{i=1}^{3}\lambda_i^2 - 3\right)\right]^n - 1\right\}, \tag{71}$$

where λ_i are principal stretches and the exponent n (>1/2) controls the degree of strain stiffening. The neo-Hookean model is recovered when n =1. Asymptotic solutions for the crack tip field have been solved for the GNH model[40,47], based on which we find the following result for steady-state crack propagation in a pure shear specimen:

$$W \approx \frac{G}{2n\pi}\frac{1}{Y}\underbrace{\sin\Theta\left(\sqrt{1-\left(1-\frac{1}{n}\right)^{2}\sin^{2}\Theta}-\left(1-\frac{1}{n}\right)\cos\Theta\right)}_{f(\Theta)}. \tag{72}$$

Interestingly, the maximum value of $f(\Theta)$ is always 1 for any n (>1/2). This result suggests that for GNH materials,

$$W_{\max}(Y) \approx \frac{G}{2n\pi}\frac{1}{Y} \quad . \tag{73}$$

which allows us to estimate the G_D and thus Γ_D (e.g. using eq.(33)). This indicates the nonlinearity of the bulk stress-strain relation, represented by n, may affect Γ_D by influencing the crack tip deformation field.

In many practical material systems, however, both the crack tip field and nonlinear constitutive model are difficult to determine, e.g. for soft viscoelastic materials. As pointed out by Knauss[27], a key challenge in viscoelastic fracture is the lack of knowledge in nonlinear constitutive relation and corresponding crack tip fields. Most existing analyses are based on the assumption of linear viscoelasticity and the *K*-field of linear elastic fracture mechanics[16,22,24]. In this case the fracture toughness becomes dependent on the crack velocity. Despite the difference in material behavior, the approach we used to derive Γ/Γ_0 for Mullins effect can also be used to derive similar formulas for linear viscoelasticity. In particular, the scaling relation $\Gamma/\Gamma_0 = 1/(1-\alpha h_{rup})$, which was developed in Zhang et al.[28] and elaborated in our work, is very similar to the result derived in de Gennes[16] and Persson[24]. Especially, like in those works we started with an additive decomposition of G: $G = G_0 + G_D$ and ended up with a multiplicative decomposition (G proportional to G_0) because G_D is itself proportional to G, as G sets the mechanical fields near the crack tip (though this is rigorously proved only in the elastic and linearly viscoelastic cases). For viscoelastic materials with strong nonlinear effects, more efforts are needed to understand the relation between fracture and dissipation[20]. For such practical materials, G_0 need not be any more a material constant, as was assumed in this work for simplicity.

Appendix 1 Connection with the Eshelby energy momentum tensor

Here we derive eq.(14) that relates the global energy release rate G to the Eshelby energy momentum tensor. We start from eq.(10) and write the following two identities based on the steady state condition:

$$\int_{\Omega} \mathbf{T}\bullet\frac{\partial \mathbf{u}}{\partial A}d\Omega = -\frac{1}{t_0}\int_{\Omega} \mathbf{T}\bullet\frac{\partial \mathbf{u}}{\partial X_1}d\Omega = -\frac{1}{t_0}\int_{\Omega} (\mathbf{SN})\bullet\frac{\partial \mathbf{u}}{\partial X_1}d\Omega = -\frac{1}{t_0}\int_{\Omega}\left(\mathbf{S}^T\frac{\partial \mathbf{u}}{\partial X_1}\right)\bullet\mathbf{N}d\Omega, \quad \text{(A1)}$$

and

$$\left.\frac{\partial \Psi}{\partial A}\right|_{\theta} = \int_V \left.\frac{\partial \psi}{\partial A}\right|_{\theta} dV = -\frac{1}{t_0}\int_V \frac{\partial \psi}{\partial X_1}dV = -\frac{1}{t_0}\int_V \nabla_{\mathbf{X}}\bullet(\psi\mathbf{e}_1)dV = -\frac{1}{t_0}\int_{\Omega}\psi\mathbf{e}_1\bullet\mathbf{N}d\Omega \quad ,$$

(A2)

where $\mathbf{N}$ is the unit outward normal vector of the surface Ω, and $\mathbf{e}_1$ is the unit vector along X_1 direction (aligned with the undeformed crack). Substituting eqs.(A1) and (A2) into eq.(10) gives:

$$G = \frac{1}{t_0}\int_{\Omega}\left(\psi\mathbf{e}_1 - \mathbf{S}^T\frac{\partial \mathbf{u}}{\partial X_1}\right)\bullet\mathbf{N}d\Omega. \quad \text{(A3)}$$

For 2D crack geometry, e.g., a plane stress crack, the integral vanishes on the front and back surfaces of the fracture specimen and is only non-zero along the lateral surface. As a result, $d\Omega = t_0 dl$ and eq.(A3) reduces to the contour integral in eq.(14).

Next we show that eq.(17) for G_D can also be derived based on the Eshelby energy momentum tensor Ξ_{ij}. As shown in eq.(14), the global energy release G is

$$G = \int_{C_{far}} \Xi_{1j}N_j dl, \quad \text{(A4)}$$

where C_{far} is a contour containing the whole specimen and ending on both crack faces. Likewise, following the reasoning of Thomas[48,49] where the crack tip is represented by a semicircle with a small but finite radius, the local energy release rate at crack tip is

$$G_0 = \int_{C_{near}} \Xi_{1j} N_j dl\,, \tag{A5}$$

where the integration contour C_{near} coincides with the semicircle representing the crack tip. If an ideal point-like crack tip is assumed, C_{near} can be considered to be infinitely close to the crack tip. Here we assume a separation of length scales, i.e. if a cohesive zone is implemented, it is much smaller than the continuum scale and thus is not visible in the region between C_{near} and C_{far}. In other words, the cohesive zone is enclosed within C_{near} and contributes only to G_0. This allows us to enforce the traction free condition for both crack faces, which leads to $\Xi_{1j}N_j$ =0 on the crack faces. Therefore, by subtracting eq.(A5) from eq.(A4) and adding two branches of integration path along the crack surface, we have

$$G - G_0 = \int_{C_{all}} \Xi_{1j} N_j dl\,, \tag{A6}$$

where C_{all} combines C_{far}, C_{near} and both crack surfaces, thereby enclosing the whole specimen but excluding the crack tip. Using the Stokes theorem, we can transform the contour integral into a surface integral:

$$G_D = G - G_0 = \int_{\Omega_a} \frac{\partial \Xi_{1j}}{\partial X_j} d\Omega\,, \tag{A7}$$

where Ω_a is the front surface of the plane stress crack specimen. Finally, using the equilibrium equation in the absence of body forces, we get

$$\frac{\partial \Xi_{1j}}{\partial X_j} = \frac{\partial \psi}{\partial X_1} - \frac{\partial}{\partial X_j}\left(S_{kj} \frac{\partial u_k}{\partial X_1} \right) = \frac{\partial \psi}{\partial X_1} - \frac{\partial F_{kj}}{\partial X_1} S_{kj} = \frac{\partial \psi}{\partial X_1} - \mathbf{S} : \frac{\partial \mathbf{F}}{\partial X_1} \,.$$

(A8)

Substituting eq.(A8) into eq.(A7) and use the pure shear fracture geometry, we obtain

$$G_D = \int_{-H_0}^{H_0} \int_{-\infty}^{+\infty} \left(-\mathbf{S} : \frac{\partial \mathbf{F}}{\partial X_1} + \frac{\partial \psi}{\partial X_1} \right) dX_1 dX_2\,, \tag{A9}$$

which is identical to eq.(17). In the literature, the contributions to $\partial \Xi_{1j}/\partial X_j$ from the various internal variables appearing in ψ are known as "local material volume forces" (up to a sign). In the present case, the integral of these local material volume forces throughout the entire specimen plane is the total dissipation concerned in this work. We emphasize that the derivation based on energy momentum tensor is already available in the literature (e.g. see pp.132–135 of Grellmann et al.[39]). Our derivation in Section 2.2 was based on direct examination of the bulk dissipation. Although the two approaches reach the same conclusion for 2D steady state crack propagation, the energetic approach in Section 2.2 is more general and is easier to interpret.

Appendix 2 Intrinsic toughness and cohesive zone

In Section 2.1, we provided a rigorous thermodynamic definition for the intrinsic toughness Γ_0, i.e. the Helmholtz free energy required to break a unit area of material. Here we follow an approach from Knauss[27,41] to prove that Γ_0 is equal to the area underneath the traction-separation curve of the cohesive zone model (see Fig.4a) for a 2D Mode-I crack. We first apply eq.(7) to the specimen shown in Fig.A1, which gives

$$t_0 \int_{C_1+C_2} \mathbf{T}\bullet\frac{d\mathbf{u}}{dt}dl - \int_V \left.\frac{d\psi}{dt}\right|_\theta dV - \Gamma_0\frac{dA}{dt} = \int_V \varphi dV\,, \tag{A10}$$

where we have applied the condition that $\mathbf{T}\cdot(d\mathbf{u}/dt)$ vanishes on the front and back surface of the specimen and replaced $d\Omega$ by $t_0 dl$ on the lateral surface. The boundary segments C_1 and C_2 are illustrated in Fig.A1. Next we apply eq.(7) to the upper half of the specimen. Since the crack tip is excluded from the sub-volume of interest, the Γ_0 term drops from the equation, which gives

$$t_0 \int_{C_1+C_4} \mathbf{T}\bullet\frac{d\mathbf{u}}{dt}dl - \int_{V_U} \left.\frac{d\psi}{dt}\right|_\theta dV = \int_{V_U} \varphi dV\,, \tag{A11}$$

where C_4 is a line segment at $X_2=0$ coinciding with the upper crack face and V_U is the volume for the upper half of the specimen. Similarly, for the lower half, we have

$$t_0 \int_{C_2+C_3} \mathbf{T}\bullet\frac{d\mathbf{u}}{dt}dl - \int_{V_L} \left.\frac{d\psi}{dt}\right|_\theta dV = \int_{V_L} \varphi dV\,, \tag{A12}$$

where C_3 is a line segment at X_2 =0 coinciding with the lower crack face and V_L is the volume for the lower half of the specimen. Adding eq.(A11) and (A12) and subtracting eq.(A10) from it, we find

$$\Gamma_0 \frac{dA}{dt} = -t_0 \int_{C_3+C_4} \mathbf{T}\bullet\frac{d\mathbf{u}}{dt}\,dl\,. \tag{A13}$$

The portions of C_3 and C_4 ahead of the crack tip coincide with each other, and thus are associated with the same displacement **u** but opposite traction **T**, which implies that the integral of **T**·(d**u**/dt) for C_3 and C_4 ahead of the crack tip cancels each other. We emphasize that the derivation until this point does not rely on the symmetry condition of Mode-I cracks, and therefore can be extended to general loading conditions (e.g. mixed-mode) or crack geometries.

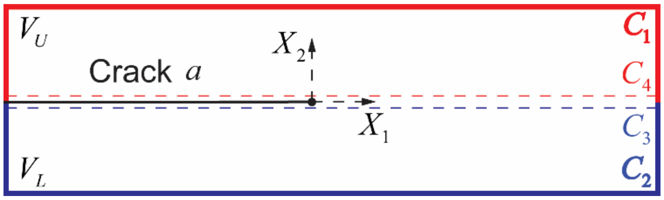

Figure A1 Schematic picture of integration segments C_1, C_2, C_3, and C_4 for a pure shear fracture specimen.

Now we are left with only the integral of **T**·(d**u**/dt) on the crack faces. Due to the symmetry condition, $\mathbf{T} = -S\mathbf{e}_2$ on the upper crack face and $\mathbf{T} = S\mathbf{e}_2$ on the lower crack face, where S is the cohesive traction and $\mathbf{e}_2$ is a unit vector along the X_2 direction. Furthermore, denoting the crack opening displacement $\delta = u_2^{(+)} - u_2^{(-)}$, i.e., the difference between vertical displacement components of the upper and lower crack faces, we can rewrite eq.(A13) as:

$$\Gamma_0 \frac{dA}{dt} = t_0 \int_{-a}^{0} S\frac{d\delta}{dt}dX_1\,, \tag{A14}$$

where a is the crack length. Finally, by using the steady state condition that (d.../dt) = (∂…/∂A) dA/dt = – (1/t_0) (∂…/∂X_1) dA/dt, we obtain

$$\Gamma_0 = -\int_{-a}^{0} S \frac{\partial \delta}{\partial X_1} dX_1 = -\int_{\delta_{\max}}^{0} S d\delta = \int_{0}^{\delta_{\max}} S d\delta, \tag{A15}$$

where $\delta_{\max}$ is the cut-off separation of the cohesive zone model. We have recovered in eq.(A15) the relation between Γ_0 and the cohesive zone model. In some cohesive zone models[50], a cut-off separation is not implemented, which can lead to a virtually unbounded cohesive zone.

Appendix 3 Additional information about FE simulations

Equation (35) for calculating W_{rup} is based on the assumption that the rupture occurs at very large deformation. Specifically, as pointed out in Long & Hui[40], in an incompressible neo-Hookean solid the material near the tip of a Mode-I crack is practically under uniaxial tension. We assume W_{rup} is associated with a large uniaxial stretch λ_{rup} (>>1):

$$W_{rup} = \frac{\mu}{2}\left(\lambda_{rup}^2 + \frac{2}{\lambda_{rup}} - 3\right) \approx \frac{\mu \lambda_{rup}^2}{2}. \tag{A16}$$

The corresponding nominal tensile stress at rupture S_{rup} is

$$S_{rup} = \mu\left(\lambda_{rup} - \frac{1}{\lambda_{rup}^2}\right) \approx \mu \lambda_{rup}. \tag{A17}$$

Next we assume S_{rup} is equal to the peak stress of the cohesive zone S_{max}. By combining eqs.(A16) and (A17), we arrive at eq.(35).

Our FE simulations are based on the explicit dynamical solver in ABAQUS, which may be sensitive to a number of simulation parameters. To ensure the FE results are independent of the simulation parameters, we performed a series of convergence tests. The results plotted using the normalized force N versus the applied stretch λ are shown in Fig.A2. In particular, we compared results using two different sets of mesh: one based on the model of Zhang et al.[28] and a finer mesh (see inset of Fig.A2a). Even though there is some deviation in the peak force, we find the two meshes give the same stretch at peak force which is the main data extracted to determine the toughness Γ. We adopted the mesh of Zhang et al.[28] since it can significantly reduce the computational time in comparison to the finer one. The rest of the simulation parameters are discussed below.

- Damping factor (Fig.A2b): the result converges and we used a value of 0 in all our simulations.
- Strain rate (Fig.A2c): it can affect the branch after the peak force by influencing the crack propagation velocity, but the effect on the location of peak force is negligible. We set the strain rate to be 2.5×10^{-3}/s to reduce computational time.
- Poisson's ratio (Fig.A2d): in the explicit dynamical solver of ABAQUS, the Poisson's ratio cannot be exactly set to 0.5 to achieve incompressibility. We found that the result converges as the Poisson's ratio approaches 0.5. Therefore, we set the Poisson's ratio to be 0.4998 in our simulations.

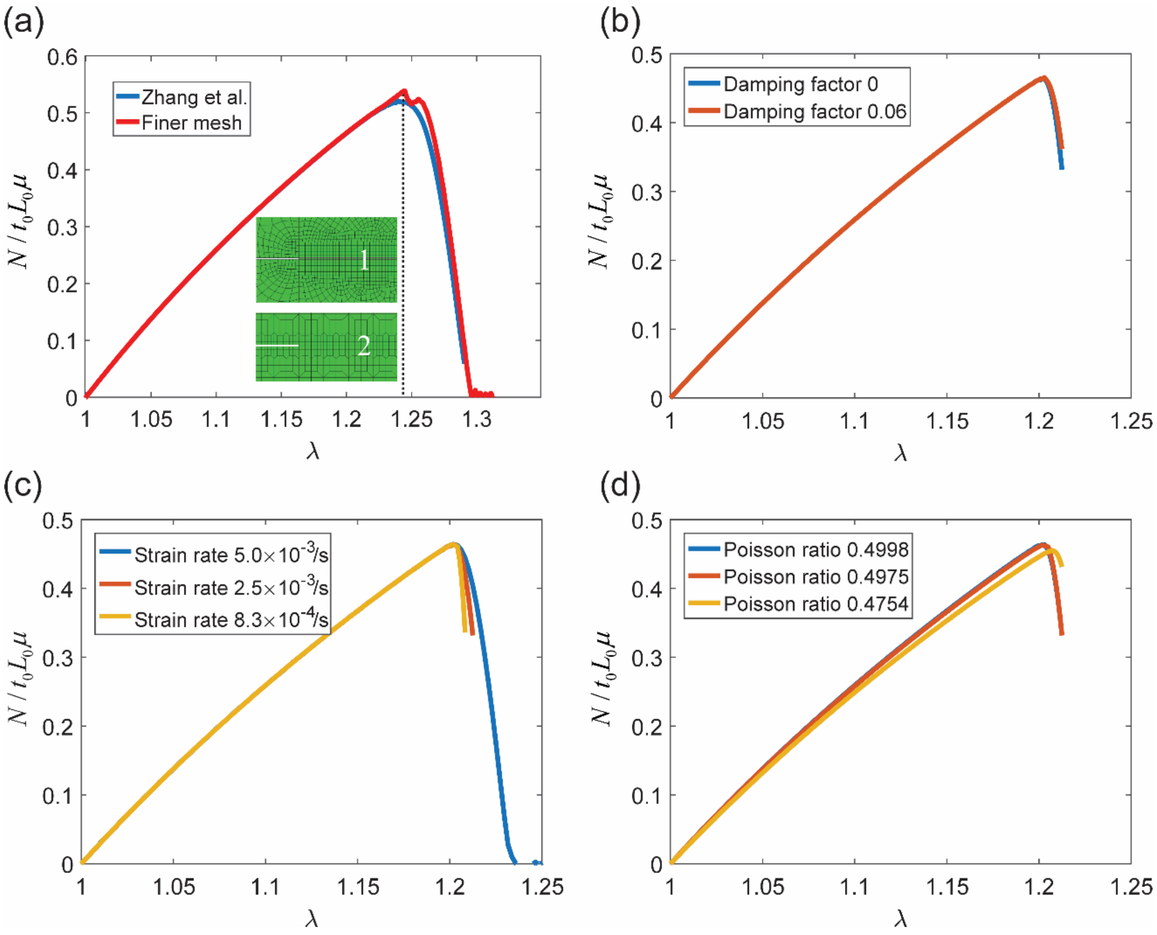

Figure A2 Results of the convergence tests for various finite element simulation parameters: (a) mesh; (b) damping factor; (c) strain rate; (d) Poisson's ratio. The inset in (a) shows snapshots of the two meshes near the crack tip in the reference configuration: Mesh 1: finer mesh; and Mesh 2: the mesh used in Zhang et al.[28]. These results are for a case with $S_{max}/\mu=4$, $\delta_{max}/H_0=0.05$, and $m/W_{rup}=0.1$.

Acknowledgement

Y.Q. and R.L. are supported by a CAREER award from National Science Foundation (CMMI-1752449). R.L. also acknowledges the support from the Michelin Chair program for a visiting professorship at ESPCI Paris, France. J.C. thanks J. Guilie, D. Berghezan, R. Schach and F. Guidolin for fruitful discussions.

References

1. Creton, C. Pressure-sensitive adhesives: An introductory course. *MRS Bull.* **28,** 434–439 (2003).
2. Morin, S. A. *et al.* Camouflage and Display for Soft Machines. *Science (80-.).* **337,** 828–832 (2012).
3. Park, S.-J. *et al.* Phototactic guidance of a tissue-engineered soft-robotic ray. *Science* **353,** 158–62 (2016).
4. Yasuda, K. *et al.* Biomechanical properties of high-toughness double network hydrogels. *Biomaterials* **26,** 4468–4475 (2005).
5. Keplinger, C. *et al.* Stretchable, Transparent, Ionic Conductors. *Science (80-.).* **341,** 984–987 (2013).
6. Lin, S. *et al.* Stretchable Hydrogel Electronics and Devices. *Adv. Mater.* **28,** 4497–4505 (2016).
7. Gao, H., Ji, B., Jager, I. L., Arzt, E. & Fratzl, P. Materials become insensitive to flaws at nanoscale: lessons from nature. *Proc. Natl. Acad. Sci. U. S. A.* **100,** 5597–600 (2003).
8. Qin, Z. & Buehler, M. J. Flaw Tolerance of Nuclear Intermediate Filament Lamina

under Extreme Mechanical Deformation. *ACS Nano* **5,** 3034–3042 (2011).

9. Zhang, T., Li, X., Kadkhodaei, S. & Gao, H. Flaw Insensitive Fracture in Nanocrystalline Graphene. *Nano Lett.* **12,** 4605–4610 (2012).

10. Chen, C., Wang, Z. & Suo, Z. Flaw sensitivity of highly stretchable materials. *Extrem. Mech. Lett.* **10,** 50–57 (2017).

11. Gong, J. P., Katsuyama, Y., Kurokawa, T. & Osada, Y. Double-network hydrogels with extremely high mechanical strength. *Adv. Mater.* **15,** 1155–1158 (2003).

12. Sun, J.-Y. *et al.* Highly stretchable and tough hydrogels. *Nature* **489,** 133–136 (2012).

13. Sun, T. L. *et al.* Physical hydrogels composed of polyampholytes demonstrate high toughness and viscoelasticity. *Nat Mater* **12,** 932–937 (2013).

14. Ducrot, E., Chen, Y., Bulters, M., Sijbesma, R. P. & Creton, C. Toughening Elastomers with Sacrificial Bonds and Watching Them Break. *Science (80-.).* **344,** 186–189 (2014).

15. Gent, A. N. Adhesion and Strength of Viscoelastic Solids. Is There a Relationship between Adhesion and Bulk Properties? †. *Langmuir* **12,** 4492–4496 (1996).

16. de Gennes, P. G. Soft Adhesives †. *Langmuir* **12,** 4497–4500 (1996).

17. Haraguchi, K. & Takehisa, T. Nanocomposite hydrogels: A unique organic-inorganic network structure with extraordinary mechanical, optical, and swelling/De-swelling properties. *Adv. Mater.* **14,** 1120–1124 (2002).

18. Huang, T. *et al.* A novel hydrogel with high mechanical strength: A macromolecular microsphere composite hydrogel. *Adv. Mater.* **19,** 1622–1626 (2007).

19. Zhao, X. Multi-scale multi-mechanism design of tough hydrogels: building dissipation into stretchy networks. *Soft Matter* **10,** 672–87 (2014).

20. Creton, C. & Ciccotti, M. Fracture and adhesion of soft materials: A review. *Reports on Progress in Physics* **79,** 46601 (2016).

21. Lake, G. J. & Thomas, A. G. The Strength of Highly Elastic Materials. *Proc. R. Soc. A Math. Phys. Eng. Sci.* **300,** 108–119 (1967).

22. Hui, C.-Y., Xu, D.-B. & Kramer, E. J. A fracture model for a weak interface in a viscoelastic material (small scale yielding analysis) Rheology of a dual crosslink self-healing gel: Theory and measurement using parallel-plate torsional Scaling of fracture energy in tensile debonding of viscoe. *J. Appl. Phys.* **721,** (1992).

23. Greenwood, J. A. The theory of viscoelastic crack propagation and healing. *J. Phys. D. Appl. Phys.* **37,** 2557–2569 (2004).

24. Persson, B. N. J. & Brener, E. A. Crack propagation in viscoelastic solids. *Phys. Rev. E - Stat. Nonlinear, Soft Matter Phys.* **71,** 36123 (2005).

25. Brown, H. R. A model of the fracture of double network gels. *Macromolecules* **40,** 3815–3818 (2007).

26. Tanaka, Y. A local damage model for anomalous high toughness of double-network gels. *EPL* **78,** 56005 (2007).

27. Knauss, W. G. A review of fracture in viscoelastic materials. *Int. J. Fract.* **196,** 99–146 (2015).

28. Zhang, T., Lin, S., Yuk, H. & Zhao, X. Predicting fracture energies and crack-tip fields of soft tough materials. *Extrem. Mech. Lett.* **4,** 1–8 (2015).

29. Ogden, R. W. & Roxburgh, D. G. A pseudo-elastic model for the Mullins effect in filled rubber. *Proc. R. Soc. A Math. Phys. Eng. Sci.* **455,** 2861–2877 (1999).

30. Holzapfel, G. A. *Nonlinear solid mechanics. A Continuum Approach for Engineering*. (Wiley, 2000).

31. Lavoie, S. R., Long, R. & Tang, T. Rate dependent fracture of a double cantilever beam with combined bulk and interfacial dissipation. *Int. J. Solids Struct.* **75–76,** 277–286 (2015).

32. T.L.Anderson. *Fracture mechanics : fundamentals and applications*. (2004).

33. Rivlin, R. S. & Thomas, A. G. Rupture of rubber. I. Characteristic energy for tearing. *J. Polym. Sci.* **10,** 291–318 (1953).

34. Haque, M. A., Kurokawa, T., Kamita, G. & Gong, J. P. Lamellar bilayers as reversible sacrificial bonds to toughen hydrogel: Hysteresis, self-recovery, fatigue resistance, and crack blunting. *Macromolecules* **44,** 8916–8924 (2011).

35. Long, R. & Hui, C.-Y. Fracture toughness of hydrogels: measurement and interpretation. *Soft Matter* **12,** 8069–8086 (2016).

36. Eshelby, J. D. The Force on an Elastic Singularity. *Philos. Trans. R. Soc. A Math. Phys. Eng. Sci.* **244,** 87–112 (1951).

37. Eshelby, J. D. The elastic energy-momentum tensor. *J. Elast.* **5,** 321–335 (1975).

38. Geubelle, P. H. & Knauss, W. G. Finite strains at the tip of a crack in a sheet of hyperelastic material: I. Homogeneous case. *J. Elast.* **35,** 61–98 (1994).

39. Grellmann, W. *et al. Fracture Mechanics and Statistical Mechanics of Reinforced Elastomeric Blends*. **70,** (Springer, 2013).

40. Long, R. & Hui, C. Y. Crack tip fields in soft elastic solids subjected to large quasi-static deformation - A review. *Extrem. Mech. Lett.* **4,** 131–155 (2015).

41. Mueller, H. K. & Knauss, W. G. Crack propagation in a linearly viscoelastic strip. *J. Appl. Mech.* **38,** 483–488 (1971).

42. Saulnier, F., Ondarçuhu, T., Aradian, A. & Raphaël, E. Adhesion between a Viscoelastic Material and a Solid Surface. *Macromolecules* **37,** 1067–1075 (2004).

43. Wang, X. & Hong, W. Pseudo-elasticity of a double network gel. *Soft Matter* **7,** 8576 (2011).

44. Lavoie, S. R., Long, R. & Tang, T. A rate-dependent damage model for elastomers at large strain. *Extrem. Mech. Lett.* **8,** 114–124 (2016).

45. Zhao, X. A theory for large deformation and damage of interpenetrating polymer networks. *J. Mech. Phys. Solids* **60,** 319–332 (2012).

46. Mayumi, K., Guo, J., Narita, T., Hui, C. Y. & Creton, C. Fracture of dual crosslink gels with permanent and transient crosslinks. *Extrem. Mech. Lett.* **6,** 52–59 (2016).

47. Long, R., Krishnan, V. R. & Hui, C.-Y. Finite strain analysis of crack tip fields in

incompressible hyperelastic solids loaded in plane stress. *J. Mech. Phys. Solids* **59,** 672–695 (2011).

48. Thomas, A. G. Rupture of rubber. II. The strain concentration at an incision. *J. Polym. Sci.* **18,** 177–188 (1955).

49. Thomas, A. G. The Development of Fracture Mechanics for Elastomers. *Rubber Chem. Technol.* **67,** 50–67 (1994).

50. Hui, C. Y., Ruina, A., Long, R. & Jagota, A. Cohesive zone models and fracture. *J. Adhes.* **87,** 1–52 (2011).